SANDIA REPORT
SAND2008-5749
Unlimited Release
Printed September 2008

Validation of Thermal Models for a Prototypical MEMS Thermal Actuator

John R. Torczynski, Michael A. Gallis, Edward S. Piekos, Justin R. Serrano,
Leslie M. Phinney, and Allen D. Gorby

Prepared by
Sandia National Laboratories
Albuquerque, New Mexico 87185 and Livermore, California 94550

Sandia is a multiprogram laboratory operated by Sandia Corporation,
a Lockheed Martin Company, for the United States Department of Energy's
National Nuclear Security Administration under Contract DE-AC04-94AL85000.

Issued by Sandia National Laboratories, operated for the United States Department of Energy by Sandia Corporation.

Available to DOE and DOE contractors from
U.S. Department of Energy
Office of Scientific and Technical Information
P.O. Box 62
Oak Ridge, TN 37831

Telephone: (865) 576-8401
Facsimile: (865) 576-5728
E-Mail: reports@adonis.osti.gov
Online ordering: http://www.osti.gov/bridge

Available to the public from
U.S. Department of Commerce
National Technical Information Service
5285 Port Royal Rd.
Springfield, VA 22161

Telephone: (800) 553-6847
Facsimile: (703) 605-6900
E-Mail: orders@ntis.fedworld.gov
Online order: http://www.ntis.gov/help/ordermethods.asp?loc=7-4-0#online

SAND2008-5749
Unlimited Release
Printed September 2008

Validation of Thermal Models for a Prototypical MEMS Thermal Actuator

John R. Torczynski, Michael A. Gallis, Edward S. Piekos,
Justin R. Serrano, Leslie M. Phinney, and Allen D. Gorby

Microscale Science and Technology Department
Sandia National Laboratories
P.O. Box 5800
Albuquerque, New Mexico 87185-MS0346

Abstract

This report documents technical work performed to complete the ASC Level 2 Milestone 2841: validation of thermal models for a prototypical MEMS thermal actuator. This effort requires completion of the following task: the comparison between calculated and measured temperature profiles of a heated stationary microbeam in air. Such heated microbeams are prototypical structures in virtually all electrically driven microscale thermal actuators. This task is divided into four major subtasks. (1) Perform validation experiments on prototypical heated stationary microbeams in which material properties such as thermal conductivity and electrical resistivity are measured if not known and temperature profiles along the beams are measured as a function of electrical power and gas pressure. (2) Develop a noncontinuum gas-phase heat-transfer model for typical MEMS situations including effects such as temperature discontinuities at gas-solid interfaces across which heat is flowing, and incorporate this model into the ASC FEM heat-conduction code Calore to enable it to simulate these effects with good accuracy. (3) Develop a noncontinuum solid-phase heat transfer model for typical MEMS situations including an effective thermal conductivity that depends on device geometry and grain size, and incorporate this model into the FEM heat-conduction code Calore to enable it to simulate these effects with good accuracy. (4) Perform combined gas-solid heat-transfer simulations using Calore with these models for the experimentally investigated devices, and compare simulation and experimental temperature profiles to assess model accuracy. These subtasks have been completed successfully, thereby completing the milestone task. Model and experimental temperature profiles are found to be in reasonable agreement for all cases examined. Modest systematic differences appear to be related to uncertainties in the geometric dimensions of the test structures and in the thermal conductivity of the polycrystalline silicon test structures, as well as uncontrolled nonuniform changes in this quantity over time and during operation.

ACKNOWLEDGMENTS

The authors gratefully acknowledge the careful technical reviews of this report by Michael J. Shaw and Sean P. Kearney and the thorough programmatic reviews of this project by Joel B. Wirth and Ernest J. Garcia, all of Sandia National Laboratories.

TABLE OF CONTENTS

Acknowledgments....4
Table of Contents....5
List of Figures....6
List of Tables....7
Nomenclature....8
1. Introduction....11
    1.1. Milestone....11
    1.2. Approach....11
2. MEMS Heat-Transfer Validation Experiments....13
    2.1. Overview....13
    2.2. MEMS Test Structures for Model Validation....13
    2.3. Experimentally Measured Thermophysical Properties....15
    2.4. Experimentally Measured Temperature Profiles....17
3. Noncontinuum Gas Heat Transfer Model....25
    3.1. Overview....25
    3.2. Thermophysical Properties of Common Gases....25
    3.3. Theoretical Formulation of Gas-Phase Heat Transfer....28
    3.4. Heat Transfer Coefficient for Microbeam Geometries....29
4. Noncontinuum Solid Heat Transfer Model....35
    4.1. Overview....35
    4.2. Thermophysical Properties of Crystalline Silicon....35
    4.3. Thermophysical Properties of SUMMiT V Materials....37
    4.4. Thermal Accommodation Coefficient....42
    4.5. Theoretical Formulation of Solid-Phase Heat Transfer....43
5. Comparison of Simulations and Experiments....45
    5.1. Overview....45
    5.2. Calore: A General FEM Code for Thermal-Analysis Simulations....45
    5.3. Calore Simulations of Heat Transfer in MEMS Test Structures....46
        5.3.1. Geometry....46
        5.3.2. Solution Approach....48
        5.3.3. Computational Grids....49
        5.3.4. Typical Simulation Results....50
    5.4. Simulation and Experimental Temperature Profiles....52
    5.5. Simulation and Experimental Electrical Results....56
6. Conclusions....59
Appendix A. Sample Calore Input Deck....61
Appendix B. User Subroutine for Gas Model....69
References....71
Distribution....74

LIST OF FIGURES

Figure 1.1. SUMMiT V chevron thermal actuator (Kearney et al., 2006). 11
Figure 2.1. SUMMiT V layers and materials (SUMMiT V, 2008)....14
Figure 2.2. SUMMiT V possible topography (SUMMiT V, 2008). 14
Figure 2.3. SUMMiT V RS539 Mod5 P4 test structures (circled) on die, 6.3×3.6 mm. 14
Figure 2.4. SUMMiT V RS539 Mod5 P4 10×200 μm test structure (close-up). 14
Figure 2.5. Electrical resistivity vs. temperature for the SUMMiT V Poly4 layer. 16
Figure 2.6. Thermal conductivity vs. temperature for the SUMMiT V Poly4 layer. 16
Figure 2.7. Renishaw inVia Raman microscope with sample stage under objective. 17
Figure 2.8. Micro-Raman probe for measuring temperature profiles of heated beams. 18
Figure 2.9. Schematic layout of the vacuum and gas supply system for the experiments. 18
Figure 2.10. Close up of packaged SUMMiT die inside the Linkam stage. 19
Figure 2.11. Raman peak position and peak width vs. temperature. 20
Figure 2.12. Experimental temperature profiles for SUMMiT V RS539 Mod5 P4 beams. 23
Figure 3.1. Experimental values (White, 1984) and curve fits for nitrogen. 26
Figure 3.2. Experimental values (White, 1984) and curve fits for air. 27
Figure 3.3. Experimental values (White, 1984) and curve fits for argon. 27
Figure 3.4. Experimental values (White, 1984) and curve fits for helium. 27
Figure 3.5. SUMMiT V RS539 Mod5 P4 fixed-fixed beam: cross section for gas model. 30
Figure 3.6. Noncontinuum gas heat transfer: schematic diagram of model geometry. 30
Figure 3.7. Noncontinuum gas heat transfer: temperature field from model simulation. 33
Figure 3.8. Comparison of FEM model and DSMC: “nominal” beam set. 34
Figure 3.9. Comparison of FEM model and DSMC: “small” beam set. 34
Figure 3.10. Comparison of FEM model and DSMC: “zero-width” beam set. 34
Figure 4.1. Experimental values (Hull, 1999) and curve fits for crystalline silicon. 36
Figure 4.2. Fitting procedure to determine P4 resistivity at a single temperature. 38
Figure 4.3. Comparison of published polysilicon thermal-conductivity measurements. 39
Figure 4.4. Comparison of published Poly4 thermal-conductivity measurements to fit. 40
Figure 4.5. Comparison of assumed P4 thermal conductivity to published data and fits. 41
Figure 5.1. Typical SUMMiT V bond pad materials and geometry. 47
Figure 5.2. Extent of computational domain with respect to test structure. 47
Figure 5.3. Original bond pad (top) and modified bond pad for simulations (bottom). 48
Figure 5.4. Medium grid for Calore simulations (gas, amber; solids, see Figure 5.1). 50
Figure 5.5. Temperature field for Case 16 with unity accommodation. 51
Figure 5.6. Bond-pad temperature field with reduced color range. 51
Figure 5.7. Comparison of experimental and simulation 200-μm temperature profiles. 54
Figure 5.8. Comparison of experimental and simulation 400-μm temperature profiles. 55
Figure 5.9. Experimental and simulation voltage drop vs. current for 200 μm beam. 56

LIST OF TABLES

Table 2.1. Experimental conditions for SUMMiT V RS539 Mod5 P4 beams. 22
Table 3.1. Curve-fit parameters in SI units for properties of common gases. 26
Table 3.2. Parameters for 81 DSMC simulations of heated microbeams. 32
Table 3.3. Parameters from DSMC for noncontinuum gas-phase heat transfer coefficient. ..33
Table 4.1. Curve-fit parameters in SI units for properties of crystalline silicon.....36
Table 4.2. Parameters for aluminum, silicon dioxide, and silicon nitride at 300 K.....37
Table 4.3. Accommodation coefficient: various measured values. 42
Table 5.1. Dimensions of geometric features used in Calore computational model. 47

NOMENCLATURE

A	separation, perpendicular distance from one wall to nearest parallel wall (m)
a_i	coefficients in correlations for gas properties (SI)
B	breadth, distance from one corner to the other of finite-extent wall (m)
b_i	coefficients in correlations for solid properties (SI)
C_p	specific heat at constant pressure (J/kg·K)
c_i	dimensionless coefficients in gas heat transfer model (positive)
$\overline{c}$	molecular mean thermal speed (m/s)
d	grain size in polycrystalline silicon (m)
E	Young's modulus (Pa)
G	rectangular beam gap height to substrate (m)
H	rectangular beam height or thickness (m)
h	heat transfer coefficient at gas-solid interface (W/m^2·K)
I	electrical current (A)
$\mathbf{j}$	electrical charge flux (A/m^2)
K	thermal conductivity (W/m·K)
k_B	Boltzmann constant (1.380658×10^{-23} J/K)
k_i	coefficients in correlations for polycrystalline silicon thermal conductivity (SI)
L	rectangular beam length (m)
L_x	computational domain extent in x direction
L_y	computational domain extent in y direction
m	molecular mass (kg)
p	pressure (Pa)
Q	heating rate (W)
$\mathbf{q}$	heat flux vector (W/m^2)
q	heat flux normal to gas-solid interface (W/m^2)
R	gas constant (J/kg·K)
R	resistance (Ω)
R_B	thermal resistance, bulk (K·m^2/W)
R_G	thermal resistance, grain boundary (K·m^2/W)
R_K	thermal resistance, Kapitza (K·m^2/W)
r	resistivity (Ω·m)
S_1, S_2	factors in heat transfer coefficient h (unity or larger)
s_i	coefficients in correlation for solid electrical resistivity (SI)
T	temperature (K)
T_A	temperature of substrate (K)
T_B	temperature of beam (K)
t	time (s)
V	electrical potential or voltage (V)
W	rectangular beam width (m)
$\mathbf{x}$	position vector (m)
x, y, z	Cartesian position coordinates (m)

α	coefficient of thermal expansion (1/K)
Γ	dimensionless sum of squares of differences (positive)
Γ_{Raman}	FWHM of Raman peak (1/cm)
γ	specific heat ratio (positive number)
λ	molecular mean free path (m)
μ	viscosity (Pa·s)
ν	Poisson's ratio (positive)
ρ	mass density (kg/m^3)
σ	thermal accommodation coefficient (0-1)
ζ	number of molecular internal energy modes (nonnegative)
Ω	center frequency of Raman peak (1/cm)
$(\ldots)_{amb}$	ambient value
$(\ldots)_{bulk}$	bulk value
$(\ldots)_{ref}$	reference value
$(\ldots)_{s}$	solid value
$(\ldots)_{tot}$	total value
$(\ldots)_{0}$	nominal value
ASC	Advanced Simulation and Computing
CTE	Coefficient of Thermal Expansion
DSMC	Direct Simulation Monte Carlo
FEM	Finite Element Method
FWHM	Full Width at Half Maximum
MEMS	MicroElectroMechanical System
MMPOLY	MicroMachined POLYcrystalline silicon
MP	Massively Parallel
NNSA	National Nuclear Security Administration
PCB	Printed Circuit Board
P&EM	Physical and Engineering Models
P0	Poly0
P1	Poly1
P12	Poly12
P2	Poly2
P3	Poly3
P4	Poly4
RS	Reticle Set
SACOX	SACrificial OXide
SOI	Silicon On Insulator
SUMMiT V	Sandia Ultra-planar Multi-level MEMS Technology V

1. INTRODUCTION

1.1. Milestone

This report documents technical work performed to complete the ASC P&EM Level 2 Milestone 2841: **Validation of thermal models for a prototypical MEMS thermal actuator.** This effort requires completion of the following task: **The comparison between calculated and measured temperature profiles of a heated stationary microbeam in air.**

Such heated microbeams are prototypical structures in virtually all electrically-driven microscale thermal actuators, as in Figure 1.1 (Kearney et al., 2006). Electrical current carried by the beams (indicated by arrows) heats the beams and causes them to expand and push the shuttle.

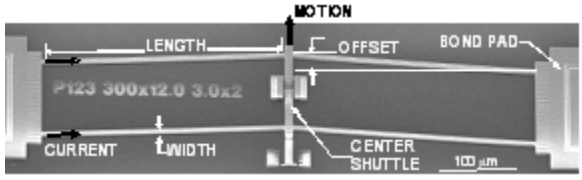

Figure 1.1. SUMMiT V chevron thermal actuator (Kearney et al., 2006).

1.2. Approach

The above task is divided into four major subtasks.

1. **Validation experiments.** Prototypical heated stationary beams are selected for study. Material properties such as thermal conductivity and electrical resistivity are measured if not known. Temperature profiles along the beams are measured as a function of electrical power and gas pressure. The uncertainty of each measurement technique is quantified.

2. **Gas-phase heat-transfer model.** Gases in microscale geometries exhibit noncontinuum heat-transfer behavior, including temperature discontinuities at gas-solid interfaces across which heat is flowing. Models are developed to enable ordinary FEM heat-conduction codes to represent these effects with reasonable accuracy for typical MEMS situations.

3. **Solid-phase heat transfer model.** Solids in microscale geometries exhibit noncontinuum heat-transfer behavior, including an effective thermal conductivity that depends on device geometry and grain size. Models are developed to enable ordinary FEM heat-conduction codes to represent these effects with reasonable accuracy for typical MEMS situations.

4. **Comparison of simulations and experiments.** Combined gas-solid heat-transfer simulations using these models are performed for the experimentally investigated devices using the ASC FEM code Calore. The simulation and experimental temperature profiles are compared to assess model accuracy.

2. MEMS HEAT-TRANSFER VALIDATION EXPERIMENTS

2.1. Overview

Prototypical heated suspended-bridge test structures were selected for study. Material properties such as thermal conductivity and electrical resistivity were measured if not known. Temperature profiles along the beams were measured as a function of electrical power and gas pressure. The uncertainty of each measurement technique was quantified.

2.2. MEMS Test Structures for Model Validation

Suspended-bridge, fixed-fixed-beam test structures were fabricated using the SUMMiT V™ (Sandia Ultra-planar Multilevel MEMS Technology) process (Sniegowski and de Boer, 2000) for use in the experiments. The SUMMiT V process uses four structural polysilicon layers (MMPOLY) with a fifth layer as a ground plane, as shown schematically in Figure 2.1. These layers are separated by sacrificial oxide layers (SACOX) that are etched away during the final release step. The upper two structural layers, Poly3 and Poly4, are nominally 2.25 μm in thickness, while the bottom two, Poly1 and Poly2, are nominally 1.0 μm and 1.50 μm in thickness, respectively. The ground plane, Poly0, is 0.300 μm in thickness and lies above a 0.800 μm layer of silicon nitride and a 0.630 μm layer of silicon dioxide (SiO_2). The sacrificial oxide layers between the structural layers are each roughly 2.0 μm thick (Sniegowski and de Boer, 2000). The SUMMiT V™ process enables the design and manufacture of complex multilayer microsystems, as illustrated in Figure 2.2.

The thermal test structures were previously used for thermal-conductivity measurements (Phinney et al., 2006; Phinney et al., 2007) and fabricated as part of reticle set 539 (RS539) module 5 (Mod5). The suspended-bridge thermal test structures were fabricated from the Poly4 layer and are nominally 2.25 μm thick. Thermal test structures were designed with a width of 10 μm and four lengths: 200, 300, 400, and 500 μm. A complete RS539 die is shown in Figure 2.3 with the 10×200 μm and 10×400 μm thermal test structures circled. The base of the fixed-fixed beam ends at bond pads, layered structures that mechanically anchor the beam to the substrate and provide a location for wire bonding to a package. An optical microscope image of a 10×200 μm thermal test structure is shown in Figure 2.4.

The beam widths were measured using the focused Raman laser beam, 0.5 μm diameter, and the automated Prior stage on the Renishaw inVia system. The resolution of the Prior stage is 0.1 μm. The widths were also measured using image analysis of high-magnification images of the beams. These techniques indicate a beam width of 9.67±0.15 μm (very close to the nominal value of 10.0 μm in Figure 2.4). An interferometer was used to measure the height of the upper beam surface (the top of the P4 layer) above the surrounding substrate. The height of thermal test structures was 14.20±0.05 μm (slightly higher than the nominal value of 13.00 μm in Figure 2.1). These measured values are used when developing the solid model for computing coupled gas-solid heat transfer.

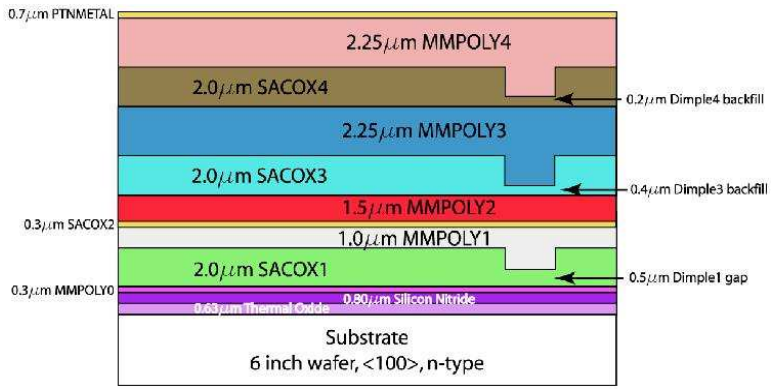

Figure 2.1. SUMMiT V layers and materials (SUMMiT V, 2008).

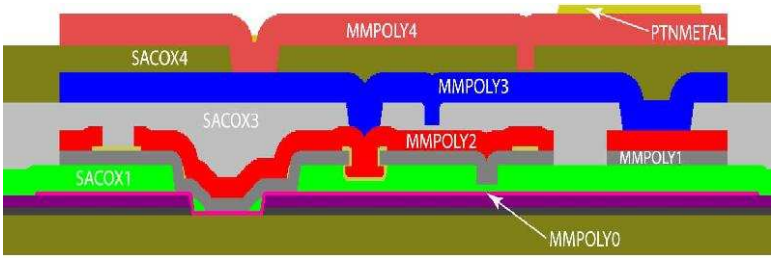

Figure 2.2. SUMMiT V possible topography (SUMMiT V, 2008).

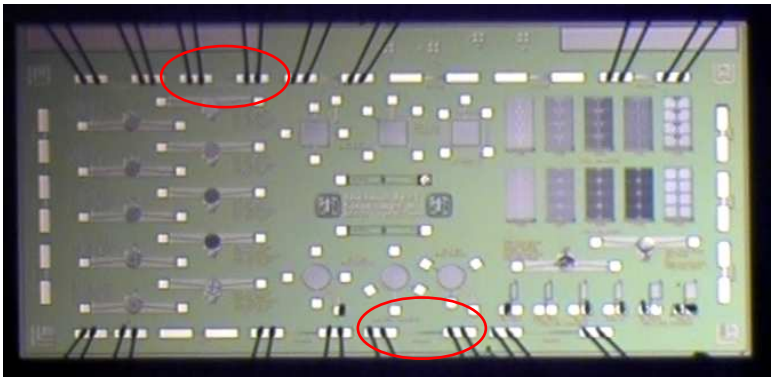

Figure 2.3. SUMMiT V RS539 Mod5 P4 test structures (circled) on die, 6.3×3.6 mm.

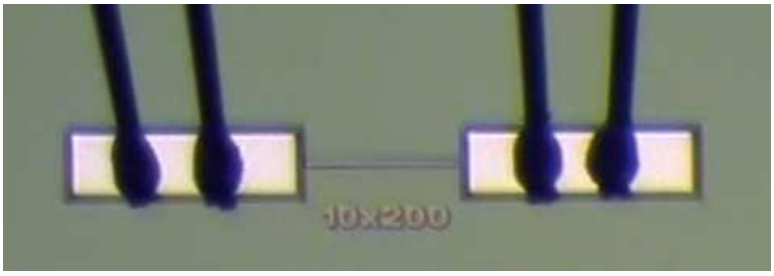

Figure 2.4. SUMMiT V RS539 Mod5 P4 10×200 μm test structure (close-up).

2.3. Experimentally Measured Thermophysical Properties

The electrical resistivity and the thermal conductivity were measured using suspended-bridge test structures that are similar to the RS539 thermal test structures. They were fabricated as part of reticle set 485 (RS485) module 5 (Mod5) (Phinney et al., 2006). A brief description of the measurements is provided here, and more detailed information is provided in Phinney et al. (2006). The experiments were performed in cryostats to control the temperature between 83 K and 575 K.

The electrical resistance was measured using a four-point probe technique in which the current was sourced through the outer leads and the voltage was monitored using the inner leads. The electrical resistivity was calculated for the 10×200 μm Poly4 thermal test structures assuming a 2.25 μm thickness and neglecting the impact of 5 μm fillets at the base of the beams. The resulting electrical resistivity for the Poly4 layer is shown in Figure 2.5. The electrical resistance measurements contain the lead and bond wire resistances, so the electrical resistivity values are considered to be higher than the actual values with an uncertainty of around 10%.

The thermal conductivity was measured using a steady-state electrical technique in which the thermal conductivity was calculated assuming one-dimensional heat conduction in a test structure subject to electrical heating for a range of currents at a given ambient condition. The Poly4 thermal conductivity is plotted in Figure 2.6, and empirical fits to the data over two temperature ranges are given in Equations 2.1 and 2.2, with all quantities in SI units so that the calculated thermal conductivity K_s is in W/m·K and the temperature T is in K. Research on the effects of bond pad heating on the thermal-conductivity measurements indicated that the uncertainty on the thermal conductivity data is around 15% (Phinney et al., 2007).

$$K_s = k_0 + k_1 T + k_2 T^2 + k_3 T^3 \text{ for } 83\text{ K} \le T \le 193\text{ K},$$
$$k_0 = 35.62111,\ k_1 = 1.594555,\ k_2 = -1.220266\times10^{-2},\ k_3 = 2.615225\times10^{-5}; \quad (2.1)$$

$$K_s = k_4 T^{k_5} + k_6 \text{ for } 193\text{ K} \le T \le 573\text{ K},$$
$$k_4 = 5.858570\times10^{3},\ k_5 = -8.139494\times10^{-3},\ k_6 = -5.535406\times10^{3}. \quad (2.2)$$

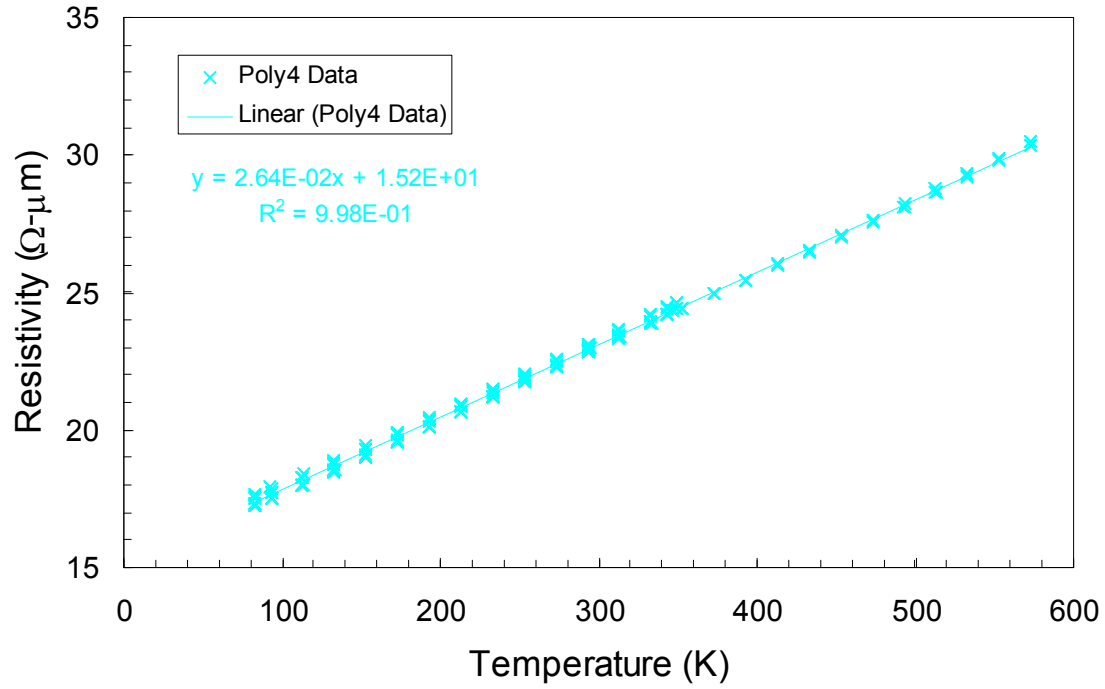

Figure 2.5. Electrical resistivity vs. temperature for the SUMMiT V Poly4 layer.

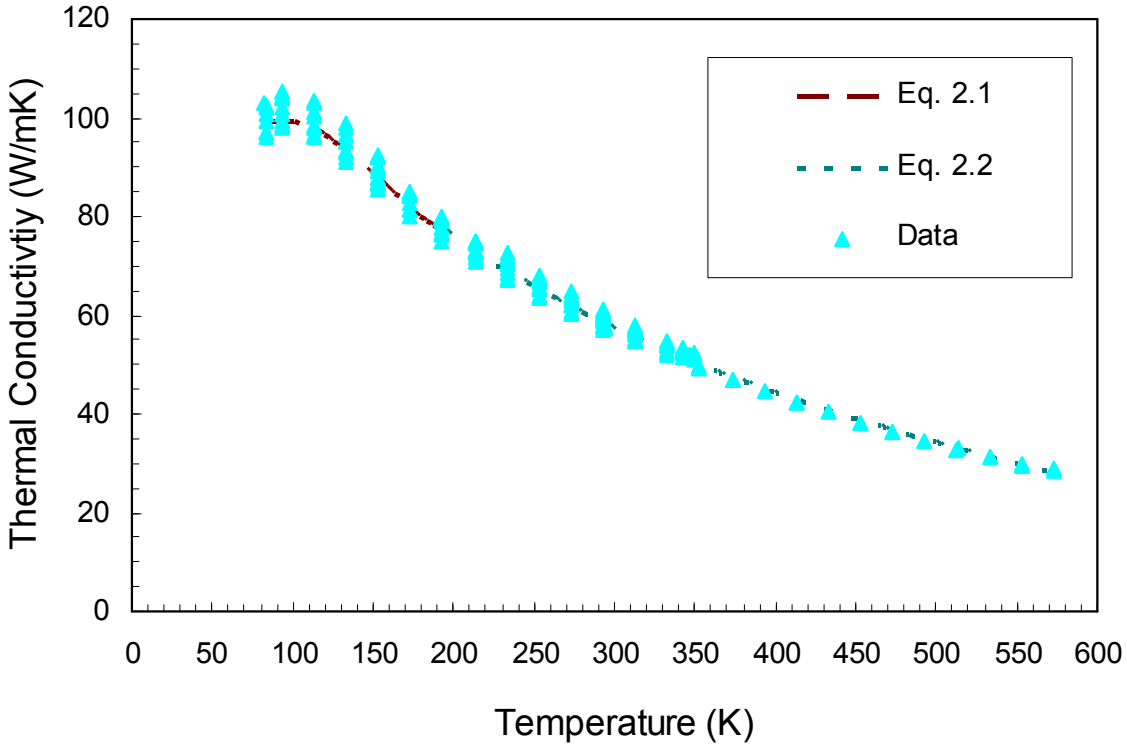

Figure 2.6. Thermal conductivity vs. temperature for the SUMMiT V Poly4 layer.

2.4. Experimentally Measured Temperature Profiles

Temperature measurements were obtained with micro-Raman spectroscopy (Kearney et al., 2006) using a Renishaw inVia Raman microscope, shown in Figure 2.7. The microscope uses a 180° backscattering geometry and a 488 nm Ar^+ laser as the probe that produces a diffraction-limited spot of 560 nm in diameter when focused by a 50×, 0.50-numerical-aperture objective, as shown in Figure 2.8. The actual measurement diameter within the sample is larger at 1.70 μm because of spreading of the probe laser within the sample. Raman signal arising from the sample surface is collected through the objective, dispersed by a grating spectrograph, and detected with a back-side illuminated, thermoelectrically cooled CCD camera (Princeton Instruments Pixis). Dispersion of the Raman signal at the CCD is 0.57 cm^{-1}/pixel.

Laser power at the sample is attenuated to 65 μW to minimize localized heating of the sample that would otherwise introduce a bias into the temperature measurement. Minimal heating of the sample is confirmed by obtaining Raman spectra at different laser powers from a room-temperature SUMMiT sample until no change in the Raman peak position was observed. Using scaling arguments presented by Kearney et al. (2006), the power deposited on the probed location, assuming full absorption and a sample thermal conductivity of 30 W/m·K (equivalent to SUMMiT polysilicon at 523 K), would amount to a temperature increase of 1.3 K; considering a silicon surface reflectivity of 39% (Aspnes and Studna, 1983), this value is likely closer to 0.8 K.

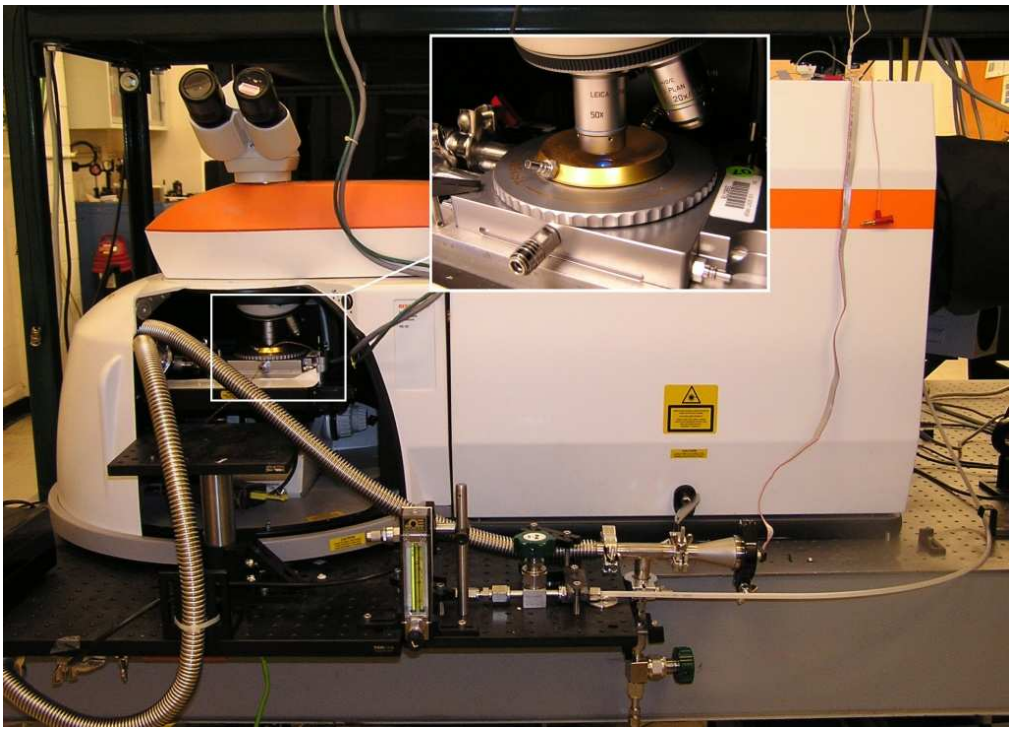

Figure 2.7. Renishaw inVia Raman microscope with sample stage under objective.

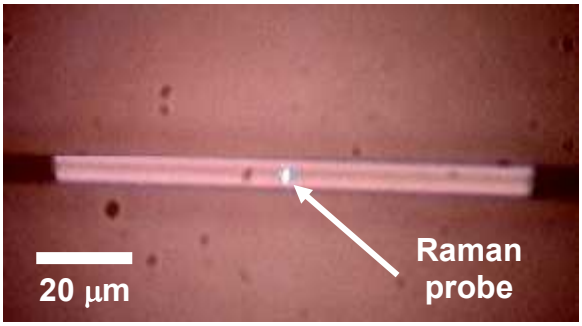

Figure 2.8. Micro-Raman probe for measuring temperature profiles of heated beams.

In the Raman process, photons from the incident probe light source interact with the optical phonon modes of the irradiated material and are scattered to higher (anti-Stokes) or lower frequencies (Stokes) from the probe line frequency. In the case of silicon and polysilicon, the scattered Raman light arises from the triply degenerate optical phonon at the Brillouin zone center. The resulting spectrum for the Stokes (lower frequency) Raman response has a single narrow peak at approximately 520 cm^{-1} from the laser line frequency at room temperature. Increases in temperature affect the frequency, lifetime, and population of the phonon modes coupled to the Raman process, leading to changes in the Raman spectra, namely a shift in the peak position and broadening of the Raman peak. Both metrics are practical for temperature mapping of MEMS. However, while peak width is sensitive only to surface temperature, peak position is sensitive to both stress and temperature (Kearney et al., 2006; Beechem et al., 2007).

For thermometry of the test beams under varying-pressure conditions, a Linkam temperature-controlled thermal stage fitted with vacuum ports was used. A diagram of the layout of the vacuum system is shown in Figure 2.9. The system used ultra-high-purity nitrogen gas as the purge gas and permitted control of the pressure inside the stage from ambient (nominally 625 torr ± 10 torr) to 0.010 torr measured with a BOC Edwards Pirani gauge. The flow rate of nitrogen into the stage was maintained at 20 cc/min for pressures above 0.05 torr, and at 6 cc/min for a pressure setting of 0.05 torr. With a chamber volume of ~30 cc, the gas exchange rate inside the chamber is 1.5 minutes at all pressures, except for 0.05 torr where it is about 5 minutes.

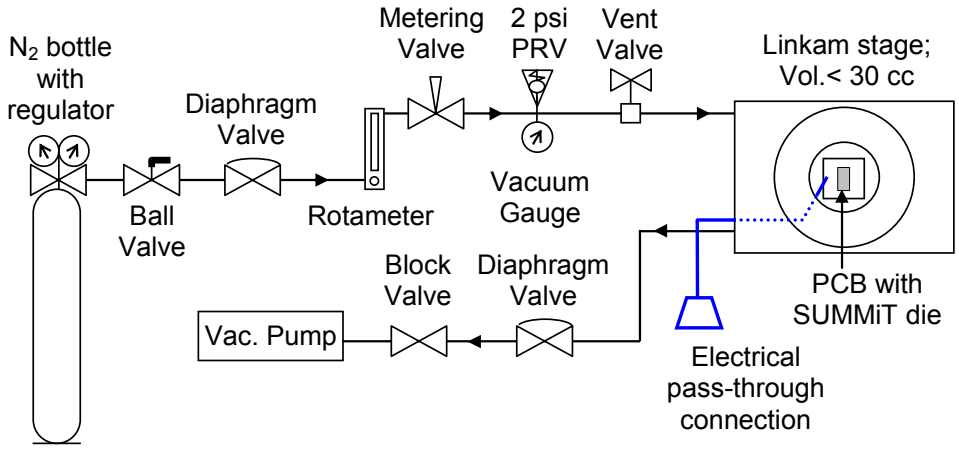

Figure 2.9. Schematic layout of the vacuum and gas supply system for the experiments.

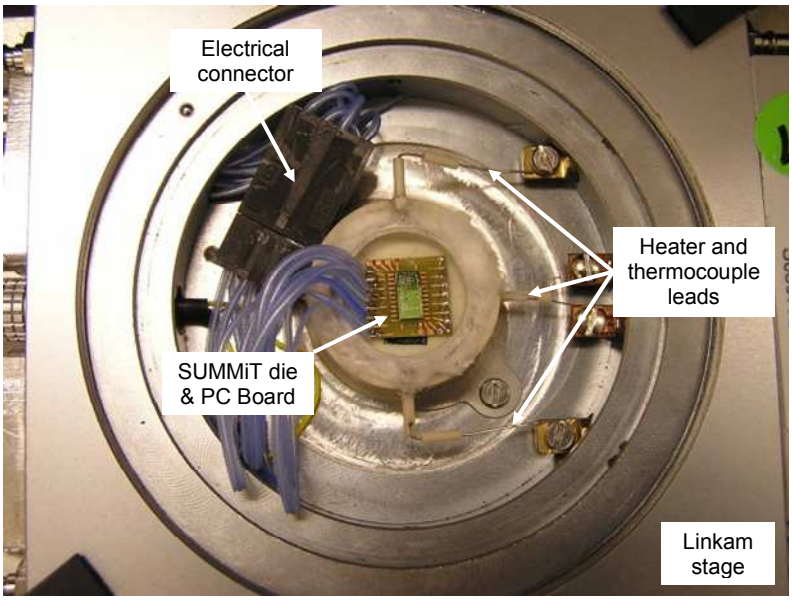

Figure 2.10. Close up of packaged SUMMiT die inside the Linkam stage.

To provide electrical power to the test devices, the SUMMiT die was packaged on a printed circuit board (PCB) to which wire leads were soldered. Each bond pad on the beam structure is wire-bonded to two separate connections on the PCB to allow for four-point sensing of the voltage. Quick-disconnect connectors were used inside the stage to allow for easy exchange of parts. The PCB was placed in the center of a quartz crucible inside the stage and held in place with vacuum-compatible carbon tape. The heating ability of the stage was used to heat the sample to a temperature of 300-310 K to ensure a consistent substrate temperature for the measurements. The devices were powered with a Keithley 2400 Source Meter in a four-point sensing configuration, where the current is flowed through the outside connections and the voltage is measured across the inner ones.

Prior to performing the measurements on the test structures, a temperature calibration of the Raman response from the Poly4 layer of an RS539 Mod5 sample was obtained by placing the die in a second temperature-controlled hot stage and acquiring Raman data over a temperature range of 300-700 K. The sample used in the calibration was from the same fabrication run as those used in the validation measurements but was a different sample altogether. A Voight function, which captures both the Lorentzian Raman line shape and the Gaussian instrument function, is fitted to the Raman spectral data to extract both the center position, Ω, and the full width at half maximum (FWHM), Γ_{Raman}, of the Raman peak (Kearney et al., 2006). At different temperatures in the calibration range, six spectra are acquired from the sample and fitted, and the extracted peak position and peak width are then averaged and plotted as a function of temperature, as shown in Figure 2.11.

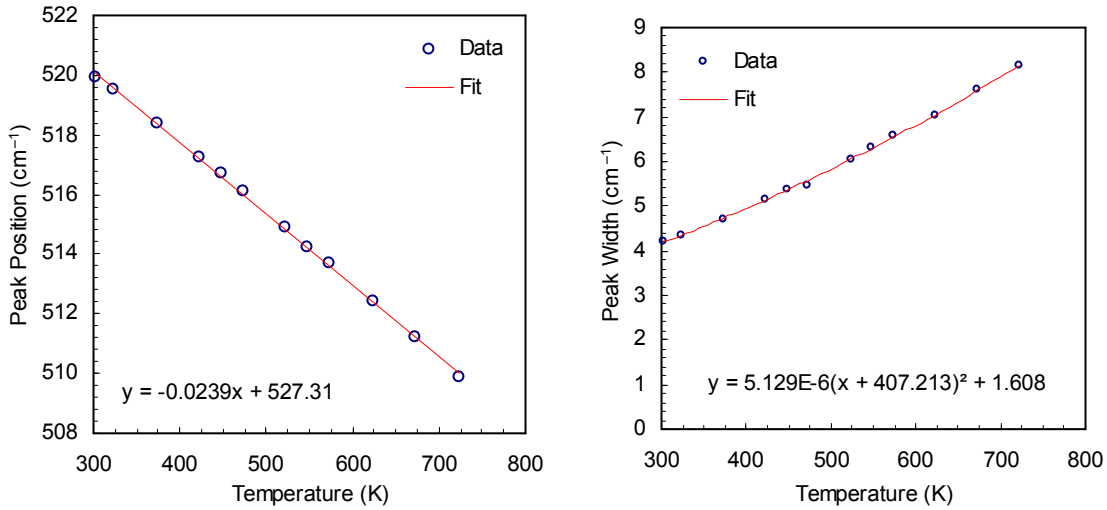

Figure 2.11. Raman peak position and peak width vs. temperature.

The data are then fitted to a calibration function that correlated the observed change in the Raman spectra to temperature. For the Raman peak position, the correlation is linear and is described by the expression

$$\Omega = \frac{\partial \Omega}{\partial T} T + \Omega_o \,, \tag{2.3}$$

where $\partial\Omega/\partial T = \left(-0.0239 \pm 0.00018\right)$ cm^{-1}/K and $\Omega_o = 527.314$ cm^{-1} and T is in K. For the Raman peak width (FWHM), the correlation is quadratic with temperature and is given by the expression

$$\Gamma_{Raman} = A\left(T + B\right)^2 + C \,, \tag{2.4}$$

where $A = 5.129 \times 10^{-6}$ cm^{-1}/K^2, $B = 407.213$ K, and $C = 1.608$ cm^{-1}. Since the RS539 Mod5 P4 fixed-fixed beams used in this study (Figure 2.4) are anchored at both ends, thermal expansion during heating is constrained, and the beams are placed under compressive stress during their operation. For this reason, peak width is used as the metric for the test, and sample temperature is extracted using Equation 2.4.

Two devices were tested for the validation measurements: a 10×200 μm beam and a 10×400 μm beam, as highlighted in Figure 2.3. The Raman temperature measurements were taken under five different pressure conditions (625, 50, 5, 0.5, and 0.05 torr) for both geometries. The electrical currents used to power the devices (see Table 2.1) were chosen so as to provide relatively consistent peak temperatures over the various pressures. The 10×200 μm beam was tested under two current conditions that would provide peak temperatures of 400-450 K and 600 K, respectively; the 10×400 μm beam was powered to provide a peak temperature of 450-500 K.

Raman spectra were collected from the powered bridge structures at regular intervals (~15 μm for 200 μm beams, ~30 μm for 400 μm beams) along the length of the structure. At every point, six acquisitions were taken with an integration time of 50-140 s per acquisition, with longer times needed for the hotter regions of the device. The peak intensity of the Raman signal (Raman + background) was maintained at 6000 CCD counts. To account for possible drift in the system, Raman data were acquired periodically (approximately every 30 μm for the 200 μm beam and every 60 μm for the 400 μm beam) from the silicon reference sample that is integrated into the inVia system. Additionally, the devices were powered off after 4-5 points, and Raman data were taken from the unpowered device.

After acquiring the Raman data, the spectra were fitted with a Voight function, and the FWHM of each Raman peak was extracted. The peak width values were then converted into temperatures using Equation 2.4. Plots of temperature as a function of position along the tested beam are shown in Figure 2.12, with the corresponding experimental conditions (pressure, initial temperature, current, voltage, and power) shown in Table 2.1. Error bars in Figure 2.12 represent the collective error in the measurement from the principal sources of uncertainty in the measurement, which are the accuracy of the peak width extraction and the error resulting from the temperature calibration. The peak width extraction through the curve fit was the largest source of uncertainty, with an uncertainty of ±6.58 K over the temperature range explored in the samples, as determined by taking multiple spectra at a fixed temperature during the calibration. The error contribution from the temperature calibration curve (Equation 2.4) is ±4.66 K. The contribution of system drift, although accounted for during the measurements by taking data from an unheated reference, is only ±0.03 K for peak width measurements.

An additional source of uncertainty is the variation in the pressure of the system. For the system discussed above, the uncertainty in the pressure control is ±1% of the full scale for pressures below 100 torr and 1 torr for higher pressures. Here, full scale for the vacuum gauge is taken to be the next-highest power of 10 in torr from the pressure reading (i.e., 10 torr full scale for a 5 torr pressure, with an uncertainty of ±0.1 torr). The corresponding temperature fluctuation due to these pressure variations is estimated to be no more than ±3.5 K for all pressures and conditions based on the fluctuations observed in the voltage drop across the sample with the observed pressure fluctuations.

Assuming that these uncertainties are uncorrelated yields an uncertainty for the peak-width-based temperature measurement of ±8.79 K. This total uncertainty is slightly lower than previously reported by Beechem et al. (2007), namely ~9 K rather than ~11 K, because of the increased number of acquisitions used and the increased signal level used.

An additional potential source of uncertainty is the possibility of grain growth in the central regions of the heated beams because these regions experience the highest temperatures (~700 K in some cases). Grain growth would affect the Raman measurement and uncertainty because increased long-range order would reduce the phonon lifetimes and therefore reduce the Raman peak width used as the temperature metric. However, since grain growth has not been experimentally measured, its effects are not incorporated into either the measurement or the uncertainty estimate.

Table 2.1. Experimental conditions for SUMMiT V RS539 Mod5 P4 beams.

Case (#)	Length (μm)	Pressure (torr)	Init. Temp. (K)	Current (mA)	Voltage (V)	Power (mW)
25	200	0.05	308.15	4.63	1.02411	4.74
15	200	0.05	303.15	4.63	1.02949	4.77
19	200	0.05	308.15	6.52	1.59047	10.37
26	200	0.05	303.15	6.64	1.61896	10.75
20	200	0.05	308.15	6.65	1.61960	10.77
21	200	0.5	303.15	4.65	1.03033	4.79
14	200	0.5	303.15	4.65	1.03376	4.81
18	200	0.5	308.15	6.54	1.59602	10.44
22	200	0.5	303.15	6.66	1.62404	10.82
23	200	0.5	303.15	6.66	1.62474	10.82
13	200	5	304.15	4.80	1.06870	5.13
24	200	5	303.15	6.77	1.65105	11.18
11	200	50	303.15	5.70	1.29737	7.40
12	200	50	303.15	5.70	1.29747	7.40
16	200	50	304.15	7.13	1.73995	12.41
29	200	625	303.15	5.30	1.17786	6.24
06	200	625	303.15	5.40	1.20902	6.53
10	200	625	303.15	6.00	1.36490	8.19
30	200	613	303.15	7.60	1.85132	14.07
07	200	625	303.15	7.60	1.85497	14.10
08	200	625	303.15	7.60	1.85745	14.12
33	400	0.05	298.05	3.00	1.32495	3.97
34	400	0.5	297.85	3.02	1.33297	4.03
35	400	5	297.85	3.20	1.41210	4.52
36	400	50	297.85	3.72	1.64197	6.11
32	400	625	297.85	4.20	1.85443	7.79

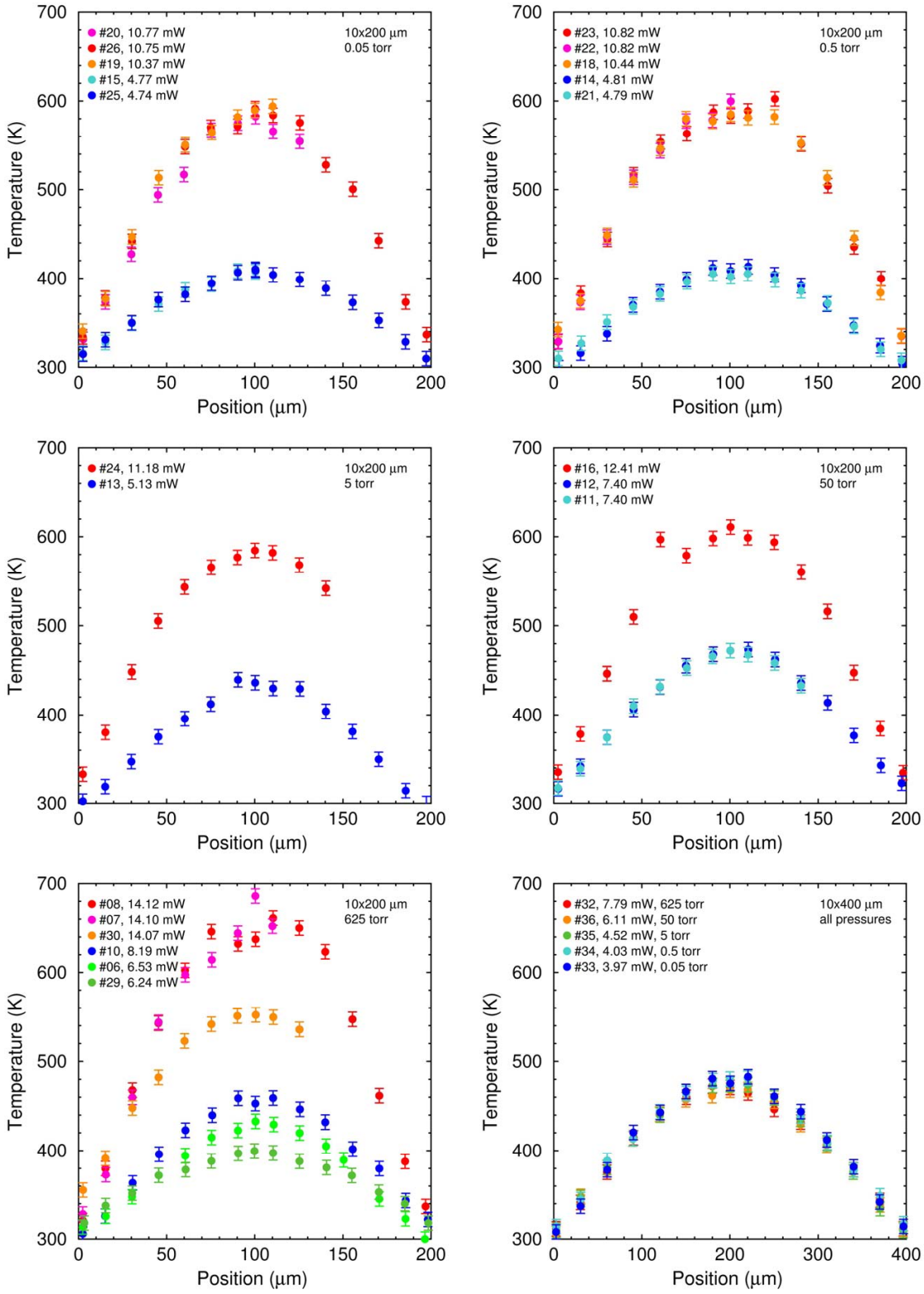

Figure 2.12. Experimental temperature profiles for SUMMiT V RS539 Mod5 P4 beams.

The plots in Figure 2.12 include not only temperature profiles but also the electrical powers corresponding to these profiles, which are also listed in Table 2.1. Comparing the top two plots in this figure, it is seen that increasing the pressure by a factor of 10 from 0.05 torr to 0.5 torr hardly changes the temperature profiles and the corresponding powers. This observation indicates that gas-phase heat transfer is negligible compared to solid-phase heat transfer at these low pressures. When the pressure is increased to 5 torr, the power must be increased by about 4% to keep the peak of the high-power temperature profile around 600 K, so gas-phase heat transfer is about 4% of solid-phase heat transfer at 5 torr. A similar comparison indicates that gas-phase heat transfer is about 15% and 31% of solid-phase heat transfer at gas pressures of 50 torr and 625 torr, respectively. Thus, gas-phase heat transfer is significant for devices of this size at ambient pressure but becomes small as the pressure is reduced.

3. NONCONTINUUM GAS HEAT TRANSFER MODEL

3.1. Overview

Gases in microscale geometries exhibit noncontinuum heat-transfer behavior, including temperature discontinuities at gas-solid interfaces across which heat is flowing. Models are developed to enable ordinary FEM heat-conduction codes to represent these effects with reasonable accuracy for typical MEMS situations.

3.2. Thermophysical Properties of Common Gases

Gas completely fills the space between the solid regions. The gas can be a mixture of different species, and these species can be monatomic (no internal energy) or polyatomic (having internal energy). The mass density ρ, the temperature T, and the pressure p are taken to be related by the ideal gas law, as in Equation 3.1, which is expressed here in terms of reference quantities, as in Equation 3.2, and the specific heat at constant pressure C_p, the thermal conductivity K, and the viscosity μ are taken to be functions of the temperature T but to be independent of the pressure p, as in Equations 3.3 and 3.4:

$$\rho = \rho_{\text{ref}} \left(\frac{p}{p_{\text{ref}}} \right) \left(\frac{T_{\text{ref}}}{T} \right); \tag{3.1}$$

$$T_{\text{ref}} = a_{01},\ p_{\text{ref}} = a_{02},\ \rho_{\text{ref}} = a_{03}; \tag{3.2}$$

$$C_p = \frac{a_{04} + a_{05}T^2 + a_{06}T^3 + a_{07}T^4}{1 + a_{08}T^3} \text{ for nitrogen and air,}$$

$$C_p = \frac{a_{04} + a_{05}T^2 + a_{06}T^3}{1 + a_{07}T^2 + a_{08}T^3} \text{ for argon and helium;} \tag{3.3}$$

$$K = \frac{a_{09}T^{a_{10}}}{1 + a_{11}T},\ \mu = \frac{a_{12}T^{a_{13}}}{1 + a_{14}T}. \tag{3.4}$$

Table 3.1 shows the parameter values in SI units corresponding to the experimental data in White (1984) for nitrogen, air, argon, and helium, and Figures 3.1-3.4 compare the curve fits and the experimental values for these gases.

Table 3.1. Curve-fit parameters in SI units for properties of common gases.

Symbol	Nitrogen	Air	Argon	Helium
a_{01}	0.30000000E+03	0.30000000E+03	0.30000000E+03	0.30000000E+03
a_{02}	0.10132500E+06	0.10132500E+06	0.10132500E+06	0.10132500E+06
a_{03}	0.11390000E+01	0.11770000E+01	0.16230000E+01	0.16270000E+00
a_{04}	0.10498477E+04	0.10070444E+04	0.54000000E+03	0.51970000E+04
a_{05}	-.31372958E-03	-.23565566E-03	0.24810683E-01	0.00000000E+00
a_{06}	0.32105536E-05	0.38074224E-05	0.20843033E-03	0.00000000E+00
a_{07}	0.40934953E-10	0.14656980E-09	0.47704728E-04	0.00000000E+00
a_{08}	0.24142120E-08	0.31415653E-08	0.40044252E-06	0.00000000E+00
a_{09}	0.13115075E-04	0.10046364E-04	0.89869560E-05	0.70752774E+10
a_{10}	0.16223709E+01	0.15980930E+01	0.15768086E+01	0.17493518E+01
a_{11}	0.14279190E-01	0.83845722E-02	0.10286123E-01	0.34531643E+13
a_{12}	0.12594024E-07	0.13144373E-07	0.13654655E-07	0.31125371E-07
a_{13}	0.15044133E+01	0.15076292E+01	0.14981922E+01	0.16450445E+01
a_{14}	0.91694406E-02	0.94944092E-02	0.69690532E-02	0.58582248E-01

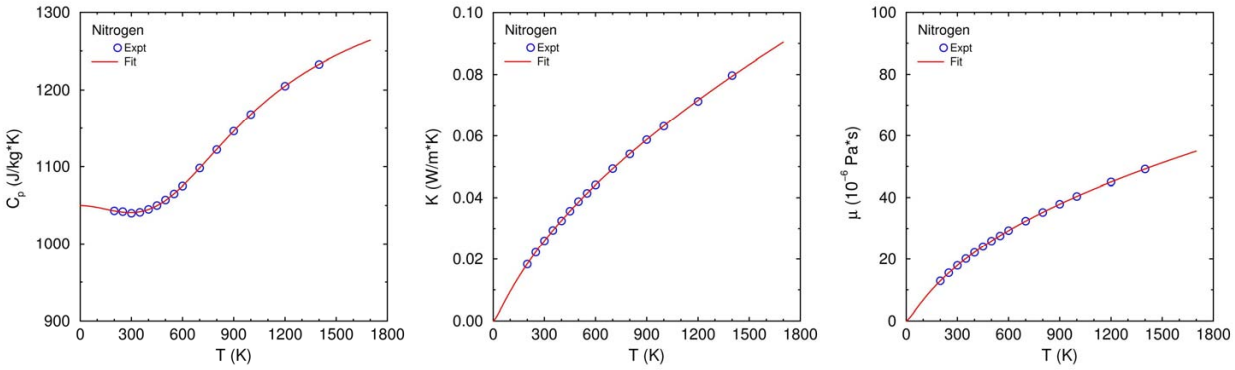

Figure 3.1. Experimental values (White, 1984) and curve fits for nitrogen.

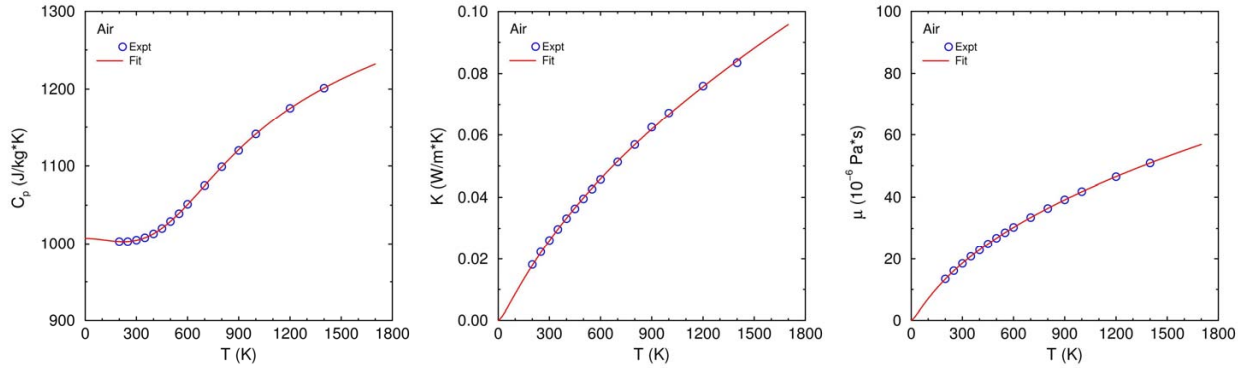

Figure 3.2. Experimental values (White, 1984) and curve fits for air.

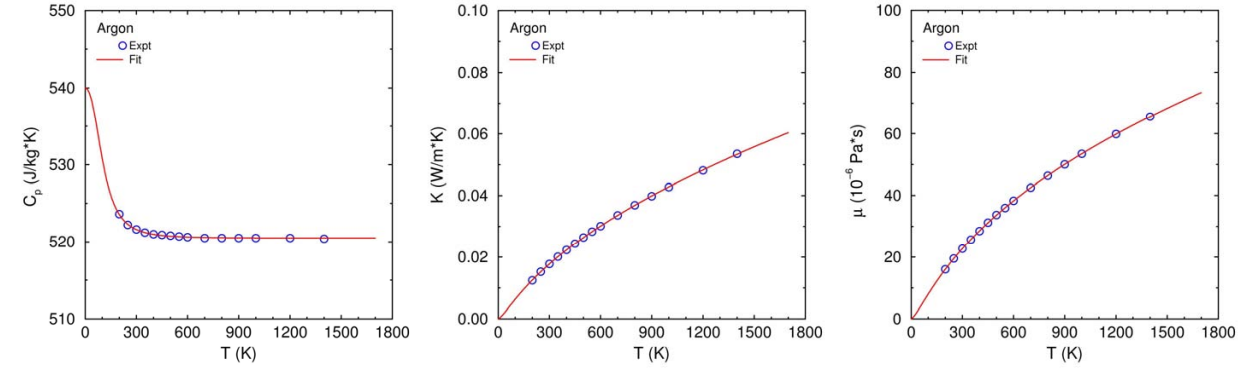

Figure 3.3. Experimental values (White, 1984) and curve fits for argon.

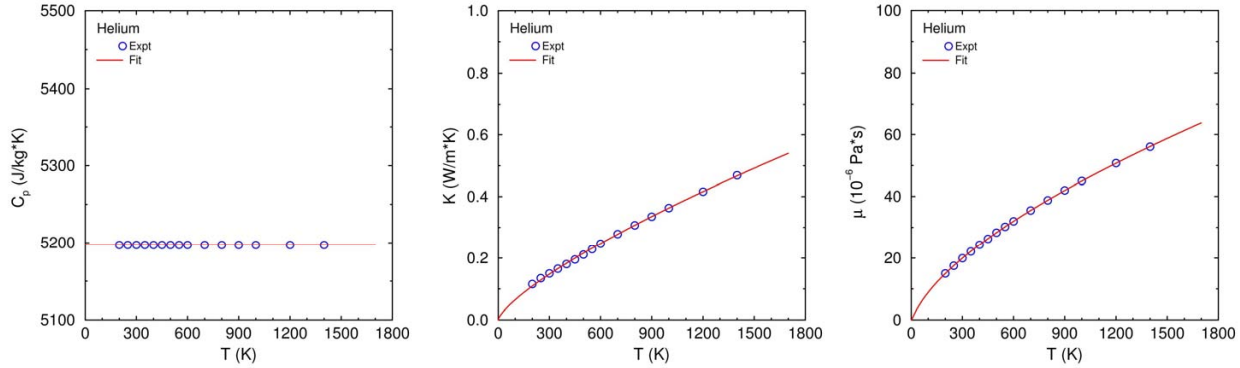

Figure 3.4. Experimental values (White, 1984) and curve fits for helium.

3.3. Theoretical Formulation of Gas-Phase Heat Transfer

The following theoretical formulation is selected to represent noncontinuum microscale gas-phase heat transfer. See Gallis et al. (2007) for additional information.

1. **Ideal gas.** The mass density ρ is related to the pressure p and the temperature T by the ideal gas law, and the viscosity μ, the thermal conductivity K, and the specific heat at constant pressure C_p depend on the temperature T but not on the pressure p. This assumption is reasonable because pressures are generally no higher than atmospheric and temperatures are generally no lower than room temperature so that the gas is thus dilute. While convenient, this assumption can be relaxed if needed.

2. **Quasi-steady heat transfer.** Temporal variations enter only through boundary conditions at gas-solid interfaces. This assumption is reasonable because a temperature difference across a gap of 1 μm typically relaxes on the order of 10 ns, which is much shorter than other time scales. Again, while convenient, this assumption can be relaxed if needed.

3. **Motionless gas.** The gas is considered to be stationary. This assumption is reasonable whenever the time scale describing the motion of microscale structures (if there is any) is long compared to the time scale over which temperature differences in the gas relax. Thermally induced buoyant flows are of minimal importance for microscale geometries. Again, while convenient, this assumption can be relaxed if needed.

4. **Uniform constant pressure.** The pressure p is uniform in space and constant in time. Under quasi-steady conditions, spatial and temporal variations of the pressure are small. This assumption is particularly appropriate when the microscale geometry is in contact with ambient pressure, as is typically the case for MEMS devices.

5. **Conduction heat transport.** The heat flux vector in the bulk gas obeys Fourier's law. This assumption is one of the two critical assumptions. Fourier's law is known to be accurate in the continuum (high-pressure) limit and is known to be inaccurate in the noncontinuum (low-pressure) limit. When combined with the next assumption, this assumption allows heat fluxes to be determined accurately. However, the spatial variation of the temperature is not predicted accurately at noncontinuum (low-pressure) conditions. Nevertheless, under these conditions, the temperature becomes almost uniform locally. Since the heat flux is the quantity of greatest physical interest, it is judged acceptable to sacrifice some accuracy in predicting the temperature so as to maintain good accuracy in predicting the heat flux and to retain the well-established methodology for numerically solving heat-conduction problems.

6. **Gas-solid temperature discontinuity.** A normal heat flux at a gas-solid interface produces a temperature discontinuity between the gas and the solid that is proportional to the heat flux. This assumption is the second of the two critical assumptions. This type of boundary condition enables noncontinuum gas effects to be modeled accurately.

The following expressions embody the first four points above regarding gas-phase heat transfer:

$$R = \frac{k_B}{m} = \frac{p_{\text{ref}}}{\rho_{\text{ref}} T_{\text{ref}}},\ p = p_{\text{amb}},\ \rho = \frac{p}{RT},\ \bar{c} = \sqrt{\frac{8RT}{\pi}},\ \lambda = \frac{2\mu}{\rho \bar{c}}; \tag{3.5}$$

$$\mu = \mu[T],\ K = K[T],\ C_p = C_p[T],\ \zeta = \zeta[T] = \frac{2C_p[T]}{R} - 5. \tag{3.6}$$

The following expressions embody the last two points above regarding gas-phase heat transfer:

$$\frac{\partial}{\partial \mathbf{x}} \cdot \mathbf{q} = 0 \text{ in the bulk gas,} \tag{3.7}$$

$$\mathbf{q} = -K \frac{\partial T}{\partial \mathbf{x}} \text{ in the bulk gas and at gas-solid interfaces,} \tag{3.8}$$

$$\hat{\mathbf{n}} \cdot \mathbf{q} = h\left(T - T_{\text{solid}}\right) \text{ at gas-solid interfaces.} \tag{3.9}$$

In the above expressions, "ref" denotes a reference value, "amb" denotes an ambient value, R is the gas constant, $k_B = 1.380658 \times 10^{-23}$ J/K is the Boltzmann constant, m is the molecular mass, ρ is the mass density, p is the pressure, T is the temperature, $\bar{c}$ is the molecular mean thermal speed, λ is the molecular mean free path, μ is the viscosity, K is the thermal conductivity, C_p is the specific heat at constant pressure, ζ is the number of molecular internal energy modes (e.g., about 2 for nitrogen and air but 0 for argon and helium), $\mathbf{x}$ is the position vector, $\mathbf{q}$ is the heat flux vector, $\hat{\mathbf{n}}$ is the unit normal vector pointing out of the gas and into the solid, and h is the gas-solid heat transfer coefficient.

The gas-solid heat transfer coefficient is what enables the above formulation to represent noncontinuum gas-phase heat transfer. More specifically, it is essential to prescribe a form of h that reproduces certain limiting behaviors in order for the above representation to be accurate. These limiting regimes include free-molecular and near-continuum heat transfer, for which the mean free path λ is large and small, respectively, and the impact of the breadth B of the surface and of the separation distance A to the nearest other surface on these heat-transfer regimes. Thermal MEMS geometries typically share certain geometric features that make this possible.

3.4. Heat Transfer Coefficient for Microbeam Geometries

As discussed earlier, thermal MEMS devices fabricated using the SUMMiT V process have certain geometric features in common. These devices are composed of planar layers of uniform thickness that are separated from adjacent layers by gaps of uniform thickness, with perpendicular sides. Moreover, these devices employ long beams of rectangular cross section (see Figure 3.5). Because of the large thermal conductivity of crystalline and polycrystalline silicon, the temperature of a heated beam is nearly uniform in each cross section although the temperature can vary significantly along the length. Similarly, the substrate beneath a heated beam remains very nearly at the ambient temperature.

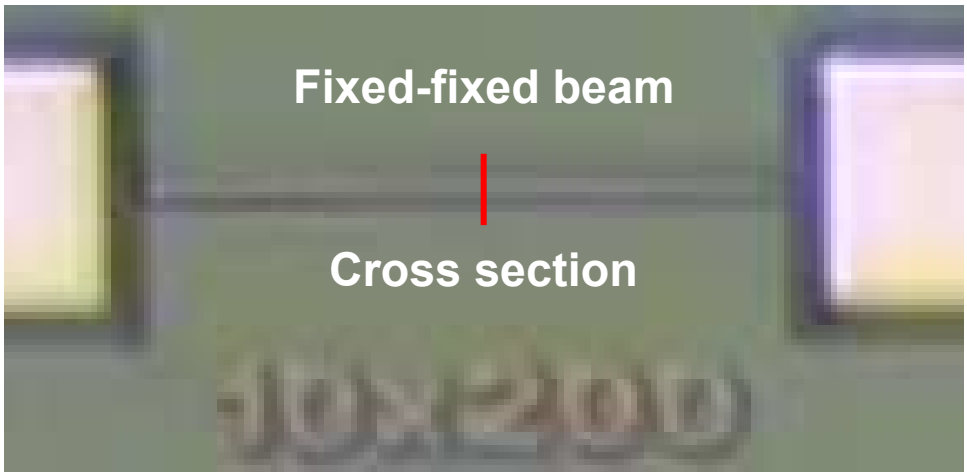

Figure 3.5. SUMMiT V RS539 Mod5 P4 fixed-fixed beam: cross section for gas model.

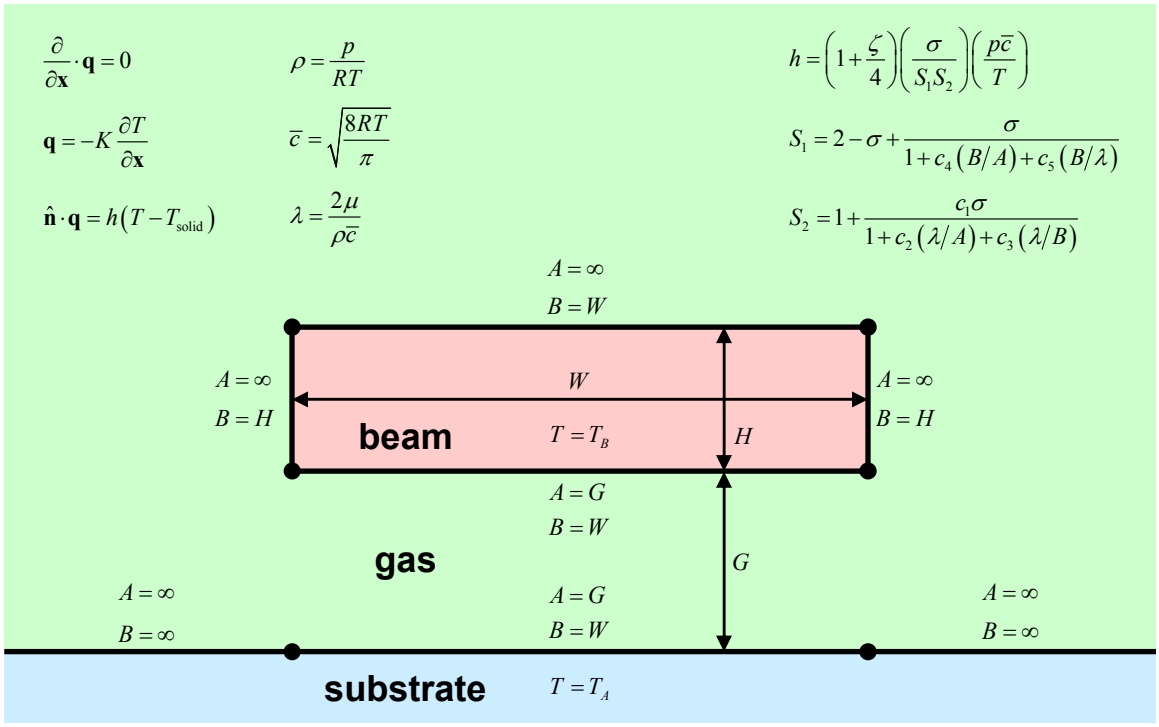

Figure 3.6. Noncontinuum gas heat transfer: schematic diagram of model geometry.

Based on these observations, the paradigmatic microscale geometry for noncontinuum gas-phase heat-transfer model development is illustrated in Figure 3.6. A beam of infinite length (out of the page) and finite width W and finite height (thickness) H is separated by a gap of uniform constant height G from a planar substrate of infinite length (out of the page) and infinite width. The beam is at uniform constant elevated temperature T_B, and the substrate is at uniform constant ambient temperature T_A. The space between the beam and the substrate is filled with gas at uniform constant pressure $p = p_{\text{amb}}$ and spatially varying temperature T that approaches the ambient temperature T_A far from the beam.

The above geometry can be further broken down into a series of line segments of finite or infinite breadth that face either an identical parallel line segment at a fixed separation or else unbounded space. Thus, each line segment in Figure 3.6 has a finite or infinite breadth B (the distance between its endpoints) and a finite or infinite separation A from a parallel segment. In Figure 3.6, the separation A and the breadth B are given for each of the 7 line segments in terms of the geometric lengths.

The following functional form of the heat transfer coefficient is prescribed for application on all gas-solid interfaces shown in Figure 3.6:

$$h = \left(1 + \frac{\zeta}{4}\right)\left(\frac{\sigma}{S_1 S_2}\right)\left(\frac{p\bar{c}}{T}\right); \tag{3.10}$$

$$S_1 = 2 - \sigma + \frac{\sigma}{1 + c_4\left(B/A\right) + c_5\left(B/\lambda\right)}, \tag{3.11}$$

$$S_2 = 1 + \frac{c_1\sigma}{1 + c_2\left(\lambda/A\right) + c_3\left(\lambda/B\right)}. \tag{3.12}$$

Here, ζ is the number of molecular internal energy modes, σ is the thermal accommodation coefficient (the probability between 0 and 1 that a gas molecule exchanges thermal energy when it reflects from a solid surface), S_1 and S_2 are order-unity dimensionless factors, A and B are the separation and breadth of a line segment, λ is the molecular mean free path, and c_1-c_5 are positive dimensionless parameters that enable S_1 and S_2 to behave correctly in limiting regimes. The above functional form reproduces known gas heat-transfer behavior in the near-continuum and free-molecular regimes for parallel-plate and isolated-body geometries (Gallis et al., 2007). The parameters c_1-c_5 control the transitions between various limiting regimes.

In the near-continuum regime, the mean free path λ is the smallest length scale, and solid surfaces have noncontinuum Knudsen layers a few mean free paths thick adjacent to them. In this regime, the limiting behaviors of S_1 and S_2 are known (Gallis et al., 2007):

$$\lambda << A << B \text{ and } \lambda << B << A: \; S_1 \to 2 - \sigma, \; S_2 \to 1 + c_1\sigma. \tag{3.13}$$

In the thin-gap regime, the separation A is the smallest length scale, and solid surfaces are separated by thin gaps much smaller than their breadth. In this regime, the limiting behaviors of S_1 and S_2 are known (Gallis et al., 2007):

$$A << \lambda << B \text{ and } A << B << \lambda: \; S_1 \to 2 - \sigma, \; S_2 \to 1. \tag{3.14}$$

In the isolated-body regime, the breadth B is the smallest length scale, and solid objects are small in extent compared to their separation from other objects. In this regime, the limiting behaviors of S_1 and S_2 are known (Gallis et al., 2007):

$$B << \lambda << A \text{ and } B << A << \lambda: \; S_1 \to 2, \; S_2 \to 1. \tag{3.15}$$

Values for the five parameters c_1-c_5 are determined by comparing model results from COMSOL (2008) simulations to results of Direct Simulation Monte Carlo (DSMC) simulations. The DSMC method represents a gas flow with computational molecules that move, collide, and reflect from solid boundaries like real molecules and is thus able to represent noncontinuum gas flows accurately (Bird, 1994).

The parameters c_1 and c_2 are determined by simulating a simplified version of the geometry shown in Figure 3.6 (Torczynski et al., 2005). In this situation, the beam width is infinite ($W \to \infty$), so there are only two solid surfaces separated by a gas-filled gap of height G. Under these circumstances, the expressions for S_1 and S_2 simplify considerably:

$$S_1 = 2 - \sigma \,,\; S_2 = 1 + \frac{c_1 \sigma}{1 + c_2 \left(\lambda / G \right)} \,. \tag{3.16}$$

Since the above situation is mathematically one-dimensional, the one-dimensional DSMC code DSMC1 is used to simulate this situation for multiple pressures spanning the range from $\lambda/G >> 1$ (low pressure, nearly free-molecular flow) to $\lambda/G << 1$ (high pressure, nearly continuum flow) for several common gases (Gallis et al., 2007). The two parameters c_1 and c_2 are adjusted until the model heat-flux values q_{FEM} match the DSMC heat-flux values q_{DSMC} as closely as possible in a least-squares sense, where normalization is used to ensure that low heat fluxes at low pressures are accurately reproduced:

$$\Gamma = \sum \left(\frac{q_{\mathrm{FEM}}}{q_{\mathrm{DSMC}}} - 1 \right)^2 \text{, where } q_{\mathrm{FEM}} = q_{\mathrm{FEM}} \left[c_1, c_2 \right]. \tag{3.17}$$

The parameters c_3-c_5 are determined by simulating the microbeam geometry shown in Figure 3.6. Sandia's DSMC code Icarus (Bartel et al., 2001) is used for these two-dimensional simulations. Three sets of beams are considered, as in Table 3.2: nominal SUMMiT V beams, "small" beams (roughly a factor of 5 smaller in all dimensions), and zero-width beams (essentially a vertical line segment of height H beginning at a height G above the substrate).

Table 3.2. Parameters for 81 DSMC simulations of heated microbeams.

Quantity	Symbol	Nominal	"Small"	Zero-Width
Beam width	W	10, 20, 50 μm	2, 4, 10 μm	0 μm
Beam height	H	2.25 μm	0.5 μm	0.5, 2, 8 μm
Beam-substrate gap	G	10.75 μm	2 μm	2 μm
Domain width, height	L_x, L_y	100 μm	100 μm	100 μm
Beam temperature	T_B	600 K	600 K	600 K
Substrate temperature	T_A	300 K	300 K	300 K
Ambient gas temperature	T_A	300 K	300 K	300 K
Gas pressure	p	10^2, 10^3, 10^4 Pa	10^2, 10^3, 10^4 Pa	10^2, 10^3, 10^4 Pa
Accommodation coeff.	σ	0.25, 0.50, 1.00	0.25, 0.50, 1.00	0.25, 0.50, 1.00

Each beam set contains three geometry variations, at least three values of the gas pressure, and three values of the thermal accommodation coefficient. Thus, there are at least 27 cases for each beam set. In all cases, the gas is nitrogen. While the parameters c_1-c_2 are held fixed, the parameters c_3-c_5 are adjusted until the model heat-loss values Q_{FEM}/L for the nominal beam set match the DSMC heat-loss values Q_{DSMC}/L as closely as possible in a least-squares sense, where normalization is used to ensure that low heat losses at low pressures are accurately reproduced:

$$\Gamma = \sum \left(\frac{Q_{\mathrm{FEM}}/L}{Q_{\mathrm{DSMC}}/L} - 1 \right)^2 \text{, where } \frac{Q_{\mathrm{FEM}}}{L} = \frac{Q_{\mathrm{FEM}}}{L}\left[c_1, c_2; c_3, c_4, c_5\right]. \tag{3.18}$$

Figure 3.7 shows a typical model temperature field, and Table 3.3 shows the parameter values from these two minimization procedures (the air values are taken to be the same as the nitrogen values because their properties are nearly identical). The minimum is fairly shallow, so varying the parameters somewhat does not affect the level of agreement significantly.

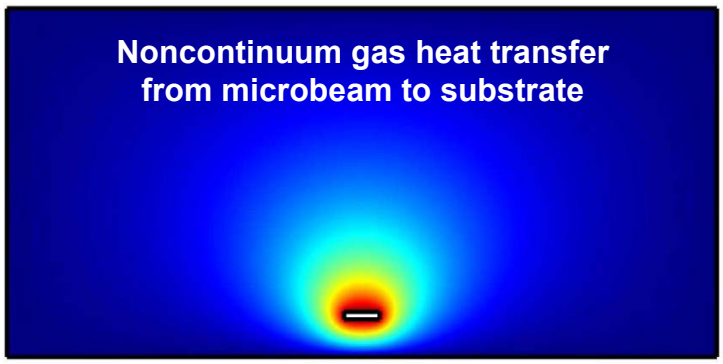

Figure 3.7. Noncontinuum gas heat transfer: temperature field from model simulation.

Table 3.3. Parameters from DSMC for noncontinuum gas-phase heat transfer coefficient.

Symbol	Nitrogen	Air
c_1	0.167	0.167
c_2	0.599	0.599
c_3	1.23	1.23
c_4	0.32	0.32
c_5	1.02	1.02

To assess its accuracy, this model is used to simulate the heat losses from the "small" and zero-width beam sets with the parameter values determined from the nominal beam sets. The zero-width beam set is a particularly severe test because its aspect ratio is different from the other two beam sets: thicker than wide, rather than wider than thick. Figures 3.8-3.10 compare the model and DSMC heat losses for all three beam sets. Excellent agreement is observed, with an RMS difference of about 3% for all cases.

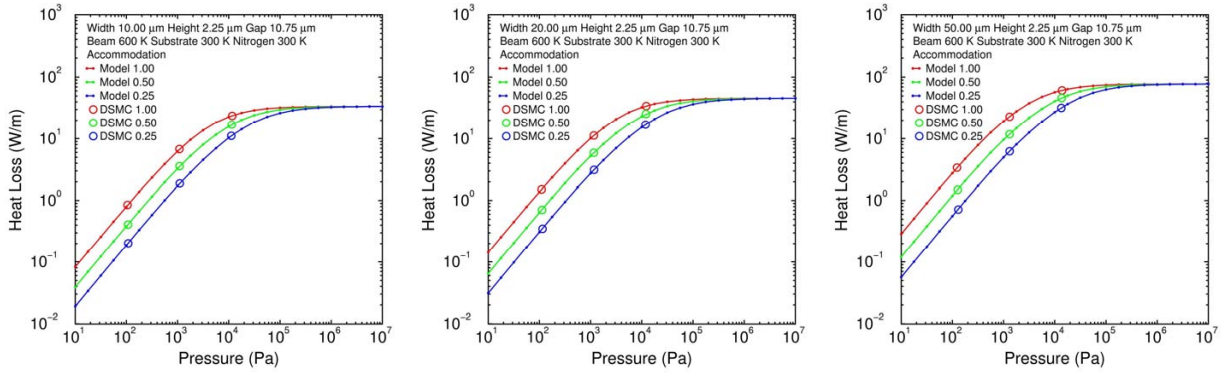

Figure 3.8. Comparison of FEM model and DSMC: "nominal" beam set.

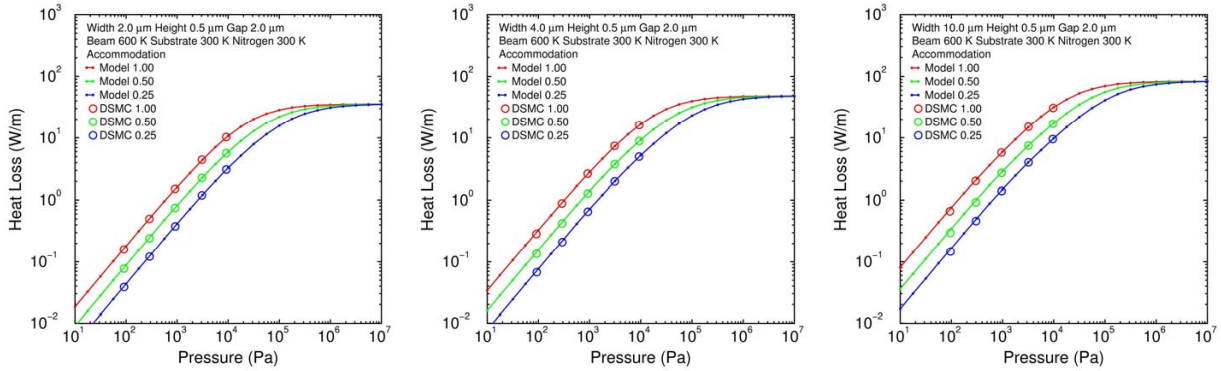

Figure 3.9. Comparison of FEM model and DSMC: "small" beam set.

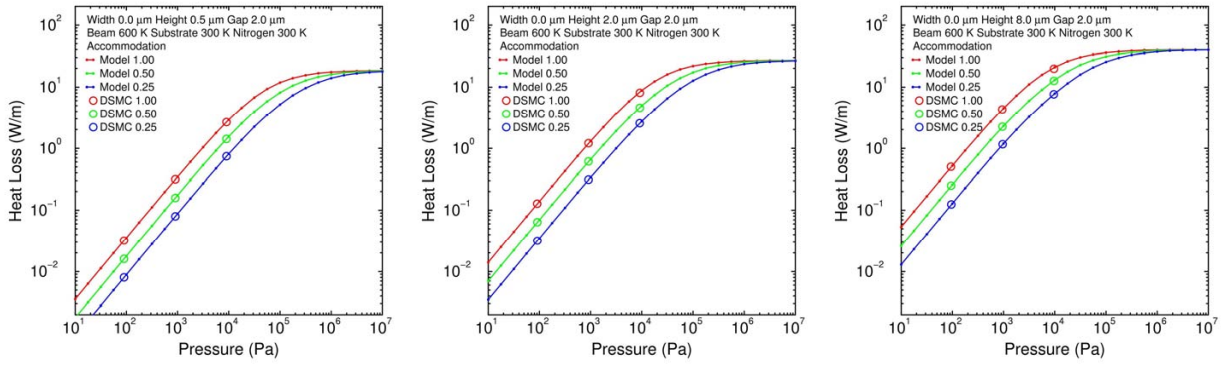

Figure 3.10. Comparison of FEM model and DSMC: "zero-width" beam set.

4. NONCONTINUUM SOLID HEAT TRANSFER MODEL

4.1. Overview

Solids in microscale geometries exhibit noncontinuum heat-transfer behavior, including an effective thermal conductivity that depends on device geometry and grain size. Models are developed to enable ordinary FEM heat-conduction codes to represent these effects with reasonable accuracy for typical MEMS situations.

4.2. Thermophysical Properties of Crystalline Silicon

MEMS devices fabricated from silicon-on-insulator (SOI) wafers have crystalline silicon both for the device layer and for the substrate layer. The mass density ρ_s, the specific heat at constant pressure C_{ps}, the thermal conductivity K_s, the coefficient of thermal expansion (CTE) α_s, Young's modulus E_s (averaged over all crystal orientations), Poisson's ratio ν_s (averaged over all crystal orientations), and the electrical resistivity r_s all depend in a complicated fashion on the temperature T but are independent of the gas pressure p (for modest pressures):

$$\rho_s = b_{01}, \tag{4.1}$$

$$C_{ps} = \frac{b_{02}T^3 + b_{03}T^4 + b_{04}T^5 + b_{05}T^6 + b_{06}T^7 + b_{07}T^8}{1 + b_{08}T^1 + b_{09}T^2 + b_{10}T^3 + b_{11}T^4 + b_{12}T^5 + b_{13}T^6 + b_{14}T^7}, \tag{4.2}$$

$$K_s = \frac{b_{15} + b_{16}T^2 + b_{17}T^3 + b_{18}T^4}{1 + b_{19}T^2 + b_{20}T^3 + b_{21}T^4}, \tag{4.3}$$

$$\alpha_s = \frac{b_{22}T^2 + b_{23}T^3 + b_{24}T^4 + b_{25}T^5 + b_{26}T^6 + b_{27}T^7}{1 + b_{28}T^2 + b_{29}T^3 + b_{30}T^4 + b_{31}T^5 + b_{32}T^6}, \tag{4.4}$$

$$E_s = b_{33} + b_{34}T\ ,\ \nu_s = b_{35} + b_{36}T\ . \tag{4.5}$$

Table 4.1 shows the parameter values in SI units corresponding to the experimental data in Hull (1999) for crystalline silicon, and Figure 4.1 compares the curve fits and the experimental values for this material. The expression below is a measured correlation for the electrical resistivity r_s produced by one particular doping profile of an SOI wafer (Tanner, 2006), where the coefficients are also shown in Table 4.1:

$$r_s = s_0 + s_1 T + s_2 T^2\ . \tag{4.6}$$

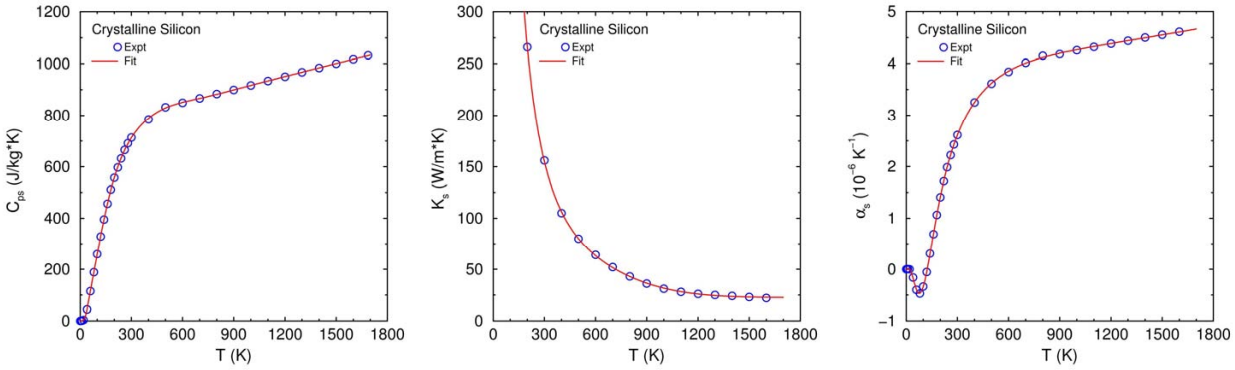

Figure 4.1. Experimental values (Hull, 1999) and curve fits for crystalline silicon.

Table 4.1. Curve-fit parameters in SI units for properties of crystalline silicon.

Symbol	Value	Symbol	Value	Symbol	Value
b_{01}	0.23290000E+04	b_{13}	-.24219655E-04	b_{25}	-.12168354E-15
b_{02}	0.30163311E+04	b_{14}	0.18993069E-07	b_{26}	0.14323759E-18
b_{03}	-.20892138E+03	b_{15}	0.12539492E+04	b_{27}	0.26640640E-22
b_{04}	0.61232060E+01	b_{16}	0.16491779E-02	b_{28}	0.43760589E-03
b_{05}	-.15080323E-01	b_{17}	-.35321754E-05	b_{29}	-.26084912E-05
b_{06}	0.98140009E-05	b_{18}	0.24055444E-08	b_{30}	0.29369668E-07
b_{07}	0.31923741E-08	b_{19}	0.12893300E-03	b_{31}	-.36085187E-10
b_{08}	0.34166502E+06	b_{20}	-.18298408E-06	b_{32}	0.44899955E-13
b_{09}	-.16235652E+05	b_{21}	0.10934293E-09	b_{33}	0.17190000E+12
b_{10}	0.32382847E+03	b_{22}	0.25572763E-09	b_{34}	-.14700000E+08
b_{11}	-.16800908E+01	b_{23}	-.15400665E-10	b_{35}	0.21930000E+00
b_{12}	0.10793247E-01	b_{24}	0.12067177E-12	b_{36}	-.26700000E-05
s_0	0.183647E-03	s_1	-.306514E-06	s_2	0.627368E-09

4.3. Thermophysical Properties of SUMMiT V Materials

The test structure contains four materials: polycrystalline silicon ("polysilicon"), silicon dioxide ("oxide"), silicon nitride ("nitride"), and aluminum. The thermophysical properties of the materials other than polysilicon are obtained from published values (see Table 4.2). These materials are deposited using reasonably standard processes, and the effects of these processes on the quantities of interest in this work are reasonably small. Resistivity values are not given for oxide and nitride because they are excluded from the electrical model.

Table 4.2. Parameters for aluminum, silicon dioxide, and silicon nitride at 300 K.

Quantity	Aluminum	Oxide	Nitride
Mass density (kg/m^3)	2702	2200	3310
Specific heat (J/kg·K)	902	740	710
Thermal conductivity (W/m·K)	235	1.4	3.2
Electrical resistivity (Ω·m)	0.028	-	-

Considerably more effort was expended to determine accurate thermophysical properties for polysilicon because these properties are critical to the current work and they vary strongly with processing conditions and with temperature.

Due to uncertainty in the fabricated resistivity and the geometry, it is not always possible to calculate an accurate beam resistance from the design. In this case, it is useful to make measurements on beams of different lengths. These data can be used to recover both the intrinsic beam resistance and the additional resistance due to connections and instrumentation by arguing that both quantities are approximately constant for a given bond pad, package, and measurement apparatus. Thus, the observed resistance R should vary according to the below expression, where L is the beam length, $\left(R/L\right)_\infty$ is the beam resistance per unit length, and R_a is the additional resistance:

$$\frac{R}{L} = \left(\frac{R}{L}\right)_\infty + \frac{R_a}{L}. \tag{4.7}$$

Because only two beam lengths were examined in this work, there are insufficient data to perform the fit with confidence. Fortunately, previous work measuring the thermal conductivity of RS539 beams in a similar apparatus (Phinney et al., 2007) provides such data. The process of fitting Equation 4.7 to this data set at 295 K by adjusting $\left(R/L\right)_\infty$ and R_a is demonstrated in Figure 4.2. This process was repeated for three samples at two temperatures. An average beam resistivity was obtained at each temperature from the corresponding $\left(R/L\right)_\infty$ value, and these resistivity values were found to be represented well by the below linear equation in temperature, where the temperature T is in K and the resistivity r_s is in Ω·μm:

$$r_s = 0.0232T + 13.6997. \tag{4.8}$$

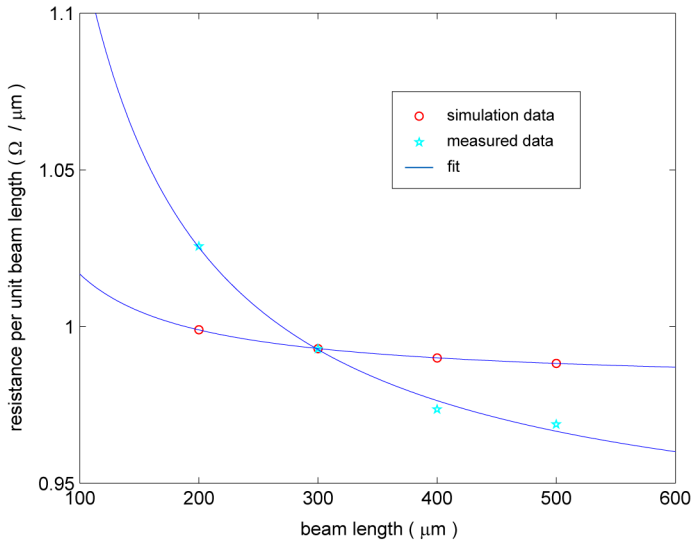

Figure 4.2. Fitting procedure to determine P4 resistivity at a single temperature.

The sheet resistance calculated from the fit using dimensions from the design guide (SUMMiT V, 2008) differs from the published nominal value for the process by only 2.4%, so it is considered reasonable. It should be noted that this fit differs from that of Figure 2.5 due to the removal of resistances outside the beam and possible run-to-run variation between RS485 (which provides the only values measured at high temperature) and RS539 (current work) structures.

To test this procedure, as well as to demonstrate that part of the additional resistance originates from the bond pad itself, simulations were performed on beams of varying lengths with a specified resistivity. The above process was then applied to the resulting data, and the results are also shown in Figure 4.2. The resistivity recovered from the fitting procedure matched the specified value to within 0.0002%.

For the thermal conductivity of polysilicon, previously presented experimental values for nominally the same structure were used in conjunction with a phenomenological argument to provide an analytical function that allows the measurements to be extended to higher temperatures and to be corrected for run-to-run variations as well as biases in the measurements, as detailed in Phinney et al. (2007).

The thermal-conductivity model is based on a series-resistance argument. A phonon traveling through a polycrystalline material is impeded by other phonons, dopants, impurities, lattice flaws, and grain boundaries. The first three factors are present in single crystal materials, whereas the last two factors are important only in polycrystalline materials.

Measurements of the thermal conductivity of crystalline silicon are available from a large number of studies over a wide temperature range, from below 100 K to the melting point at 1683 K (e.g., Holland and Neuringer, 1962; Hull, 1999; Kremer et al., 2004). These values agree to a reasonable accuracy for temperatures higher than approximately 200 K, where sample-size effects are unimportant for millimeter-scale samples. Measurements are also available for a number of polysilicon materials (e.g., Paul et al., 1994; von Arx et al., 2000; McConnell et al., 2001; Graham et al., 2003; Phinney et al., 2006; Phinney et al., 2007), but these values differ greatly, not only in their magnitude, but in the nature of their variation with temperature. The measurements from a large number of investigators are shown in Figure 4.3.

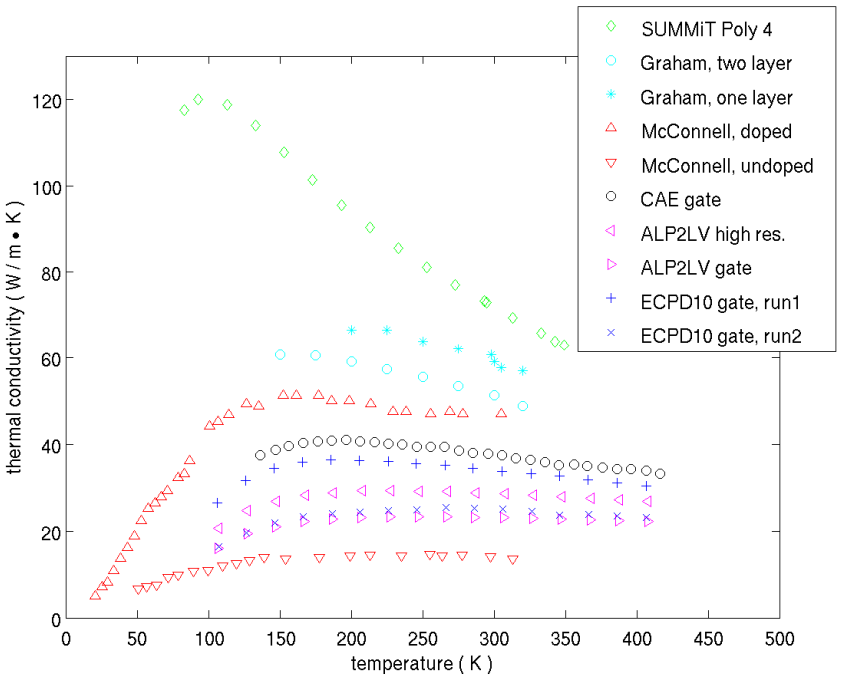

Figure 4.3. Comparison of published polysilicon thermal-conductivity measurements.

In an effort to provide a meaningful model for these measurements, the thermal resistance of a polysilicon material is expressed as large number of resistors in series, where some resistors are grain boundaries and others are chunks of bulk material. In this model, applied to polysilicon by Aubry et al. (2007), a material with two grains has two "bulk resistors" R_B and one "grain boundary resistor" R_G. The total thermal resistance R_{tot} of a material with N grains is therefore given by

$$R_{\text{tot}} = \sum_{N} R_B + \sum_{N-1} R_G \,. \tag{4.9}$$

The bulk thermal resistance is simply the inverse of the bulk thermal conductivity times the grain size d. A very simple model for K_{bulk} that agrees acceptably with the measurements in the temperature range of interest for this work is given below, where the temperature T is in K and the thermal conductivity is in W/m·K:

$$K_{\text{bulk}} = \frac{1000}{0.03T - 2} \,. \tag{4.10}$$

The grain boundary thermal resistance is simply the Kapitza resistance R_K, which has been computed and measured for a wide range of materials. Recently, the Kapitza resistance has been computed for silicon grain boundaries of several relative orientations using molecular dynamics (Aubry et al., 2008). The Kapitza resistance increases with the atomic-scale disorder of the boundary, and values of 0.08-2 K·m^2/nW have been reported in the literature.

Dividing throughout by the number of grains and taking the limit as the number of grains becomes infinite, the grain diameter becomes an average value, $\bar{d}$, and the thermal conductivity of the overall material is given by

$$K_s = \frac{1}{\frac{R_K}{\bar{d}} + \frac{1}{K_{\text{bulk}}}}. \tag{4.11}$$

The current work is complicated by the fact that none of these terms are known with certainty for SUMMiT V materials, including the bulk thermal conductivity because of the presence of dopants. In response, the Kapitza resistance divided by the grain size is considered a fitting parameter, and the bulk thermal conductivity is multiplied by a second fitting parameter (assumed less than unity).

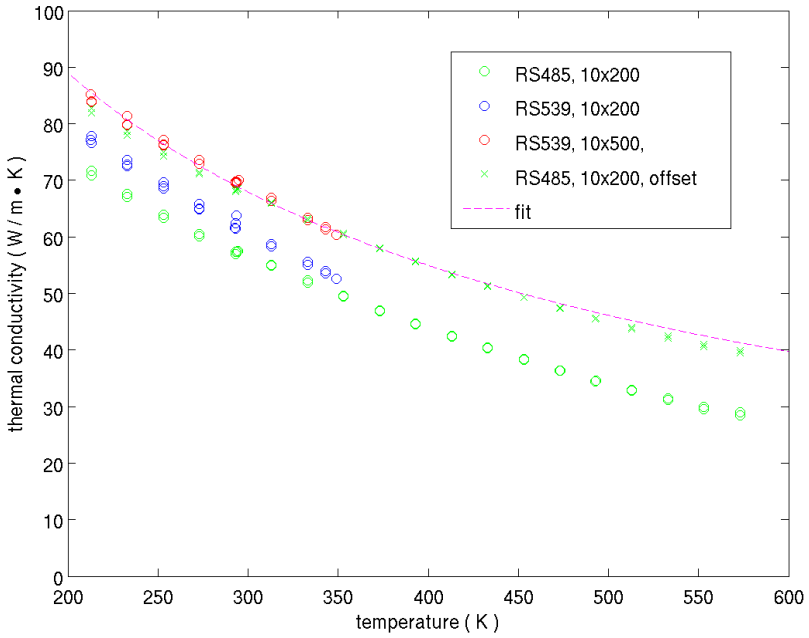

Figure 4.4. Comparison of published Poly4 thermal-conductivity measurements to fit.

While high-temperature measurements exist for the thermal conductivity of Poly4, it was measured only on 10×200 μm bridges, so the biases described in Phinney et al. (2007) cannot be estimated. Comparing these values with that of 10×200 μm and 10×500 μm bridges in Figure 4.4 demonstrates the issue. In all cases, the measurements follow a similar trend, but an offset exists between them. The offset between the RS539 data sets is an artifact of the measurement because the materials comprising the short and long bridges are largely identical. Because some of the biases identified in Phinney et al. (2007) are setup-dependent, it is possible that the difference between the RS485 and RS539 10×200 μm bridges is also an artifact although material differences are also possible because they were produced in separate runs.

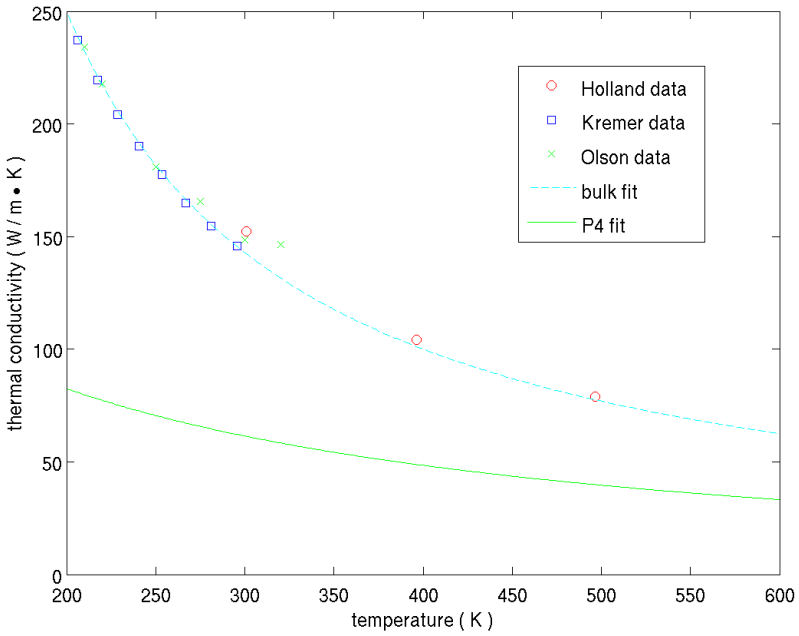

Figure 4.5. Comparison of assumed P4 thermal conductivity to published data and fits.

As a starting point, an offset was added to the measured RS485 values to bring them up to the measured RS539 10×500 μm results because Phinney et al. (2007) showed that the longest beams had the least bias error, so the 500 μm data set is closest to the true thermal conductivity. A fit was performed for Equation 4.9 on the resulting values, yielding $R_K/\overline{d} = 0.0066$ K·m/W and $K_{\text{bulk}} = 0.86K_{\text{Si}}$. Taking a midrange value of $R_K = 1\ \text{K}\cdot\text{m}^2/\text{nW}$, this result corresponds to an average grain size of $\overline{d} = 152$ nm, which lies in a plausible range for materials of this type. Similarly, a 14% reduction from typical bulk silicon thermal conductivity from non-grain-related scattering is within reason. The assumed form for the thermal conductivity therefore produces physically reasonable values for its constituent parameters.

Finally, because the offset is unknown, it was adjusted by performing simulations for Case 26, a high-power, low-pressure, 10×200 μm beam case and roughly adjusting the offset by eye to reach reasonable agreement on the peak temperature. The resulting thermal conductivity is given below, where T is in K and K_s is in W/m·K:

$$K_s = \frac{1}{0.0066 + 0.00116\left(0.03T - 2\right)} - 6.5\,. \tag{4.12}$$

This equation is plotted in Figure 4.5, along with the assumed fit for bulk thermal conductivity and a representative selection of the available measurements. Not surprisingly, the bulk and polysilicon values converge at very high temperatures, where interphonon scattering begins to dominate the overall thermal conductivity.

The temperature-dependent thermal-conductivity expression in Equation 4.12 is used without modification for all simulations shown in this work.

4.4. Thermal Accommodation Coefficient

The thermal accommodation coefficient for a particular gas-solid combination is difficult to specify for several reasons. In their compilation, Saxena and Joshi (1989) present values measured by many experimenters for a wide variety of solid-gas combinations. Table 4.3 contains their most relevant data, as well as some more recent values from Trott et al. (2009) and Arkilic et al. (2001). The glass values are included because a bare silicon surface exposed to air quickly develops a thin layer of "native oxide" (i.e., silicon dioxide, or glass). The aluminum values are included because aluminum and silicon have similar molecular weights and aluminum in air also quickly develops a thin oxide layer. The iron, steel, and gold values are included to demonstrate that the accommodation coefficients for nitrogen, oxygen, and air are often rather insensitive to the solid when the solid is a metal. The Arkilic et al. (2001) values are included because they are the only ones involving silicon even though they are for tangential momentum accommodation rather than for thermal accommodation. The fairly substantial ranges reflect a variety of factors: gas purity, surface contamination, various experimental techniques, different accommodation for translational and internal energy, dependence on solid and gas temperatures, and the difficulty of making such measurements (Saxena and Joshi, 1989).

Most experimenters treat the thermal accommodation coefficient as an adjustable parameter that is selected to bring measured and theoretical results into agreement. This same approach is adopted here. The thermal accommodation coefficient is treated as a free parameter and adjusted to bring the computational and experimental temperature profiles into as close agreement as possible. It is emphasized that only one value is to be selected and used for all cases, rather than selecting a different value for each case.

Table 4.3. Accommodation coefficient: various measured values.

Type	Solid	Gas	Range	Source
Thermal	Glass	Nitrogen	0.75-0.85	Saxena and Joshi (1989)
Thermal	Glass	Oxygen	0.77-0.84	Saxena and Joshi (1989)
Thermal	Aluminum	Air	0.87-0.97	Saxena and Joshi (1989)
Thermal	Aluminum	Nitrogen	0.84-0.88	Trott et al. (2009)
Thermal	Iron	Air	0.87-0.96	Saxena and Joshi (1989)
Thermal	Steel	Air	0.81-0.85	Saxena and Joshi (1989)
Thermal	304 SS	Nitrogen	0.85-0.89	Trott et al. (2009)
Thermal	Gold	Air	0.75-1.00	Saxena and Joshi (1989)
Thermal	Gold	Nitrogen	0.54-0.88	Saxena and Joshi (1989)
Thermal	Gold	Oxygen	0.58-0.90	Saxena and Joshi (1989)
Thermal	Gold	Nitrogen	0.81-0.85	Trott et al. (2009)
Momentum	Silicon	Nitrogen	0.78-0.88	Arkilic et al. (2001)
Momentum	Silicon	Argon	0.70-0.90	Arkilic et al. (2001)

4.5. Theoretical Formulation of Solid-Phase Heat Transfer

The following theoretical formulation represents noncontinuum microscale solid-phase heat transfer. The mass density ρ_s, the specific heat at constant pressure C_{ps}, the thermal conductivity K_s, and the electrical resistivity r_s are functions of the temperature T and other material properties, as discussed in the previous sections:

$$\rho_s = \rho_s\left[T\right],\ C_{ps} = C_{ps}\left[T\right],\ K_s = K_s\left[T\right],\ r_s = r_s\left[T\right]. \tag{4.13}$$

The temperature T is governed by transient heat conduction with resistive electrical heating produced by the charge flux $\mathbf{j}$, where Fourier's law is used for the heat flux vector $\mathbf{q}$:

$$\rho_s C_{ps}\frac{\partial T}{\partial t} = \frac{\partial}{\partial \mathbf{x}}\cdot\left(-\mathbf{q}\right) + r_s\left(\mathbf{j}\cdot\mathbf{j}\right) = \frac{\partial}{\partial \mathbf{x}}\cdot\left(K_s\frac{\partial T}{\partial \mathbf{x}}\right) + r_s^{-1}\left(\frac{\partial V}{\partial \mathbf{x}}\cdot\frac{\partial V}{\partial \mathbf{x}}\right),\ \mathbf{q} = -K_s\frac{\partial T}{\partial \mathbf{x}}. \tag{4.14}$$

The voltage V is governed by quasi-steady current flow, with temporal variations entering only through boundary conditions, where Ohm's law is used for the charge flux vector $\mathbf{j}$:

$$0 = \frac{\partial}{\partial \mathbf{x}}\cdot\left(-\mathbf{j}\right) = \frac{\partial}{\partial \mathbf{x}}\cdot\left(r_s^{-1}\frac{\partial V}{\partial \mathbf{x}}\right),\ \mathbf{j} = -r_s^{-1}\frac{\partial V}{\partial \mathbf{x}}. \tag{4.15}$$

At a gas-solid interface, the normal heat flux is proportional to the temperature difference between the solid and the gas, with the heat transfer coefficient h given in the previous chapter, and the normal charge flux is zero because the gas is an insulator, where the unit normal vector $\hat{\mathbf{n}}_s$ points out of the solid and into the gas:

$$\hat{\mathbf{n}}_s\cdot\mathbf{q} = h\left(T - T_{\text{gas}}\right),\ \hat{\mathbf{n}}_s\cdot\mathbf{j} = 0. \tag{4.16}$$

On some surfaces (e.g., electrodes), the temperature and/or the voltage may be prescribed as functions of time and/or space (perhaps constant and/or uniform):

$$T = T_{\text{prescribed}}\left[t,\mathbf{x}\right],\ V = V_{\text{prescribed}}\left[t,\mathbf{x}\right]. \tag{4.17}$$

An initial temperature distribution is required, but no initial voltage distribution is required:

$$T = T_0\left[\mathbf{x}\right]\ \text{at}\ t = 0. \tag{4.18}$$

The above equations form a closed system for heat transfer in the solid material.

5. COMPARISON OF SIMULATIONS AND EXPERIMENTS

5.1. Overview

Combined gas-solid heat-transfer simulations using these models are performed for the experimentally investigated devices using the ASC FEM code Calore. The simulation and experimental temperature profiles are compared to assess model accuracy.

5.2. Calore: A General FEM Code for Thermal-Analysis Simulations

Calore (Calore, 2006; Calore, 2008) is a massively parallel (MP) thermal-analysis simulation code developed within the SIERRA analysis-code framework at Sandia National Laboratories under the Advanced Simulation and Computing (ASC) program of the National Nuclear Security Administration (NNSA). Calore is based on the widely-used Galerkin finite element method (FEM) and supports multiple 2D and 3D element types. Calore can be used to analyze a wide range of heat-transfer situations, including but not limited to the following.

- Steady and transient heat-transfer analysis.
- Coupling to other types of analysis (e.g., electrical, structural).
- Multiple materials with properties that depend on time, position, and temperature.
- Chemical, electrical, and prescribed volumetric heating.
- Thermal resistance at interfaces, with temperature difference proportional to heat flux.
- Wide range of boundary conditions, including specified temperature, specified heat flux, specified heat transfer coefficient and ambient temperature for convective heat flux, and surface and enclosure radiation.

Calore has been used in an earlier effort to investigate noncontinuum heat transfer for microsystems (Torczynski et al., 2005). The present investigation builds on and extends the previous investigation, which also focused on noncontinuum microscale gas-solid heat transfer.

5.3. Calore Simulations of Heat Transfer in MEMS Test Structures

In order to perform Calore simulations of the complete test structure, its numerical representation must be constructed. This task includes building the geometry, meshing it, and choosing simulation parameters.

5.3.1. Geometry

While the intentionally heated portion of the test structure has a very simple geometry, its anchor points do not. These anchor points, also known as "bond pads" because they host the wire bonds for electrical connections, have complex multilayer structures because of the constraints imposed by the SUMMiT V manufacturing process (see Figure 5.1). Because cross sections of the actual devices used in this work were not available, the geometry was built based on available computational models, with some input from measured quantities.

The test structures treated in this work use a standard bond pad provided with the SUMMiT V design toolkit. The baseline three-dimensional structure for the bond pad was created from this design using the three-dimensional geometry modeler (Jorgensen et al., 2001) also provided with the SUMMiT design toolkit. This modeler is able to capture trapped oxide and other features of the manufacturing process. Several modifications were made to the baseline geometry to bring it into agreement with observed parameters and for computational efficiency.

First, the baseline bond pad, which is 52 μm × 304 μm, measured across and along the long axis of the beams, respectively, was truncated to 41 μm × 100 μm. The length was truncated because thermal contact to the substrate is made near the front edge, so most of the bond pad's length is insignificant with regard to heat transfer. Similarly, the width was truncated at the first air gap because the geometry past this point is out of the path of the primary heat flow. The full domain was then sectioned with perpendicular vertical planes crossing at the beam center point to take advantage of symmetry. The region covered in the computation is shown on a picture of the test structure in Figure 5.2.

Next, the layer thicknesses were adjusted to bring the beam height above the substrate into agreement with the interferometry measurements of the test structures used in the experiments. Because detailed information on individual layer thicknesses was not available for the present structures, the height was adjusted based on experience with previous structures (SUMMiT V, 2008). Table 5.1 shows the dimensions adopted for the computational model.

Finally, to decrease grid complexity, some minor features of the geometry were modified or deleted. First, the groove in the aluminum at the trench fill near the front of the bond pad was eliminated. This trench is meant to reflect the likelihood of gaps, either full-length or "keyholes," when filling a trench of this nature. Due to the high thermal and electrical conductivity of the aluminum compared to the other materials, the presence of this feature is unlikely to affect the overall voltage and temperature fields. The thinness of the gap, however, presents significant gridding challenges, so the decision was made to remove it. For similar reasons, the slight groove in the Poly2 layer near the trench was also removed, and the trapped oxides were trimmed slightly such that their upper edge falls at the same height as the trench floor.

A comparison of the original and modified bond pads is presented in Figure 5.3. The modified bond pad contains a small protrusion at the rear corner to simulate the wire bond location and provide a smaller area of a convenient size over which to impose a known current.

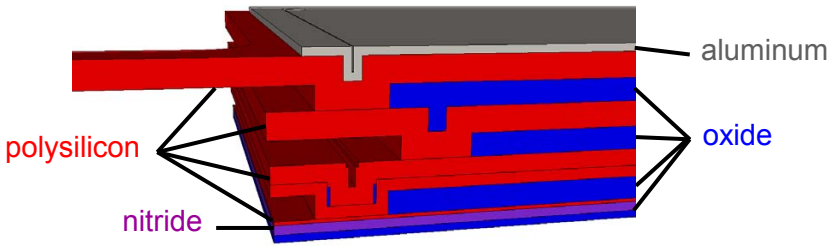

Figure 5.1. Typical SUMMiT V bond pad materials and geometry.

Figure 5.2. Extent of computational domain with respect to test structure.

Table 5.1. Dimensions of geometric features used in Calore computational model.

Layer Thickness	Model Value	Other Lengths	Model Value
Thermal Oxide	0.630 μm	Beam length (short)	200.00 μm
Silicon Nitride	0.800 μm	Beam length (long)	400.00 μm
MMPOLY0	0.300 μm	Beam width (both)	9.65 μm
SACOX1	2.000 μm	Bond pad x width	100.00 μm
MMPOLY1	1.000 μm	Bond pad y width	41.00 μm
SACOX2	0.300 μm	Gas domain y width	100.00 μm
MMPOLY2	1.260 μm	Gas domain z height	50.00 μm
SACOX3	2.461 μm		
MMPOLY3	2.320 μm		
SACOX4	2.461 μm		
MMPOLY4	2.330 μm		
PTNMETAL	0.700 μm		

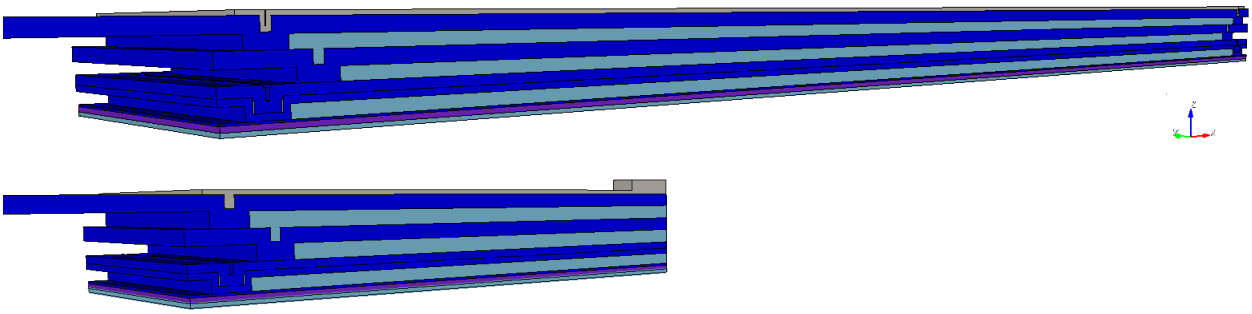

Figure 5.3. Original bond pad (top) and modified bond pad for simulations (bottom).

5.3.2. Solution Approach

Electrical heating problems are modeled in Calore by loosely coupling two calculations (known as "regions" in SIERRA): one that solves for the voltage distribution, and one that solves for the temperature distribution. The electrical calculation determines the ohmic heating, which is then provided as a volumetric heat source in the temperature calculation. The temperature calculation determines the temperature distribution, which is then provided to the electrical calculation to calculate the temperature-dependent electrical conductivity.

The coupling is governed by the "solution control" facility in SIERRA, which allows any SIERRA code to be coupled to any other SIERRA code in a user-defined manner. In this case, solution control is used to couple two Calore simulations, but it is also commonly used to couple radiation, thermal, structural, and fluids codes.

In past work, the gas model was implemented via the contact mechanism in Calore. Because the model implemented in this work depends on geometric parameters and differs for every surface involved, parameters must be passed to the model on a surface-by-surface basis. Unfortunately, the contact implementation does not currently provide a mechanism for providing data for each surface, so a different subroutine, with the data built-in, would have been required for each surface.

In order to avoid having to build a new subroutine if the geometry or accommodation coefficient was changed, a new approach was taken in the current work. In this case, the gas model was implemented via a convection boundary condition, and the solid and gas regions were solved via coupled Calore calculations. This implementation allowed all data to be passed via the input deck, freeing the user from rebuilding the subroutines (except for when a new version of Calore is released).

Because the convection coefficient depends on the gas temperature, it is computed in the gas region. To pass the result to the solid region via solution control, it must be stored on the nodes, along with the gas temperature. This is accomplished by specifying the convection coefficient subroutine as a nodal source. This subroutine then calculates and stores the nodal value of the convection coefficient, while setting its return value to zero to ensure that no actual nodal heating occurs.

A sample input deck is given in Appendix A, and a listing of the user subroutine is given in Appendix B.

5.3.3. Computational Grids

The grids for this work were generated using the Sandia meshing package CUBIT. All meshes use eight-node hexahedral elements. Where possible, the meshes were generated with the map or submap scheme because they generate high-quality elements. The remaining sections were meshed using the pave scheme, particularly the gas grid because it allowed elements to be clustered around the beam.

Due to the sudden change in electrical conductivity at the aluminum/polysilicon junction, a large voltage gradient and therefore a large ohmic heating occur at this location. Because the ohmic heating is applied on a volumetric basis centered on the nodes, it was observed that too coarse a grid in this region can cause a significant increase in the heating of the bond pad. Refining the grid does not significantly reduce the magnitude of this heating spike, but it reduces its extent, so it was generally helpful to perform local refinement in this region.

The electrical problem was solved on only the aluminum and Poly4 layers although the underlying grid was identical to that used for the thermal problem on all layers. Solving the electrical problem only on these layers decreased computation time as well as avoided difficulties caused by the very large contrast between the electrical conductivity of the conducting materials (polysilicon and aluminum) and the insulating materials (silicon dioxide and silicon nitride).

The gas heat conduction problem was solved on a mesh 100 μm wide and 50 μm tall. These dimensions were chosen by solving a steady-state, two-dimensional problem with a beam cross section held at 600 K. The domain boundaries were then placed such that the temperature gradient, and therefore the heat flux, fell below 1% of its magnitude at the beam surface at these locations, ensuring that placing insulating boundaries at these locations would have little effect on the solution. The gas grid is truncated at the base of the beam because the temperature at this point is expected to be very near ambient, so there is little expected benefit in gridding between the layers at the forward edge of the bond pad.

Grids were constructed in three levels, with uniform refinement followed by localized refinement based on the gradient in voltage for the electrical grid. The coarse mesh contained 69,543, 244,665, and 959,916 elements for the electrical, solid and gas grids, while the finest mesh contained 4,264,832, 15,472,640, and 35,318,496 elements. The medium grid is shown in Figure 5.4. Most calculations were carried out on the medium grid, which contained 540,139, 1,941,115, and 4,436,064 elements. Computation time for the three grids for Case 16 with a thermal accommodation coefficient of 0.3 (the intermediate value considered below) were 0.1, 1.3, and 5.9 hours on 50 Infiniband-connected nodes of the Sandia "Thunderbird" cluster with two 3.6 GHz EM64T processors each.

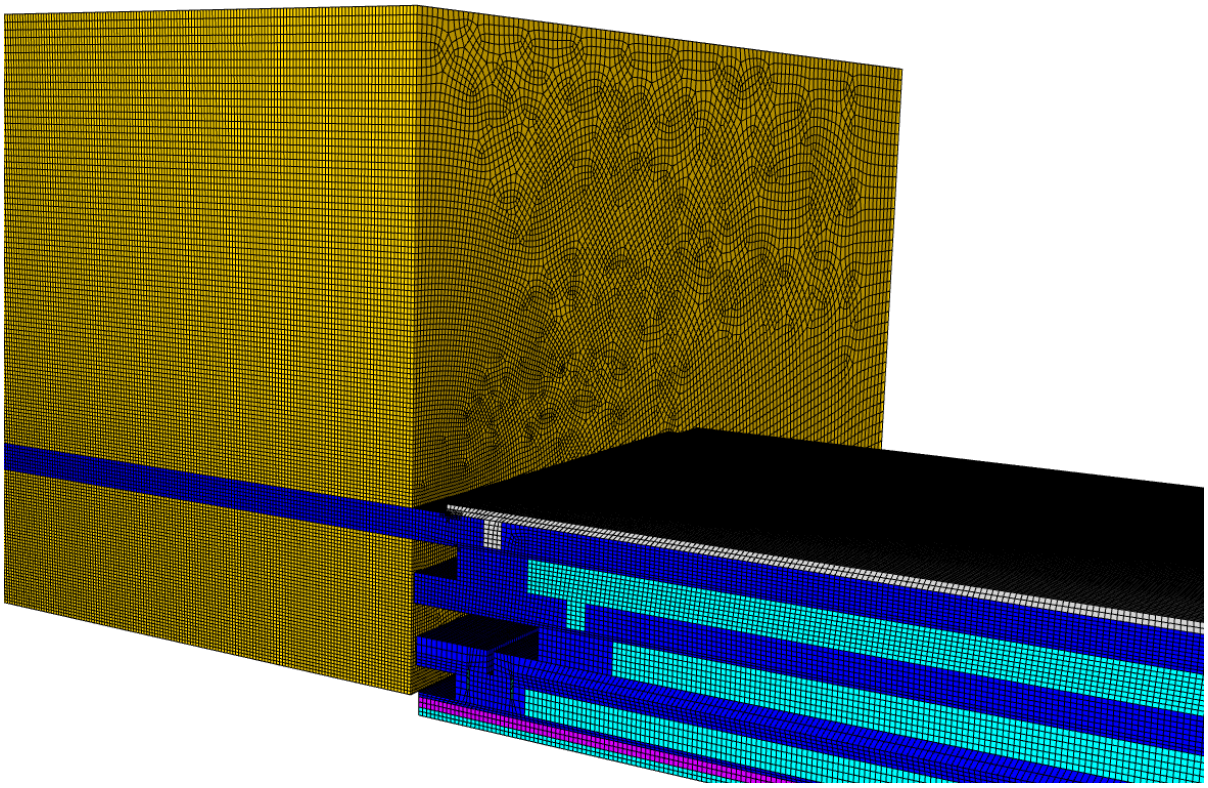

Figure 5.4. Medium grid for Calore simulations (gas, amber; solids, see Figure 5.1).

5.3.4. Typical Simulation Results

As an example of typical results, the temperature distribution in the beam and gas are shown in Figure 5.5 for Case 16 with an accommodation coefficient of unity. Several features are visible in these results. First, the beam temperature is somewhat higher than that of the adjacent gas. This is a consequence of the noncontinuum gas-solid boundary condition. Second, the highest temperature, and most of the gas-phase heat transfer to the substrate, occurs at the beam center because the ends are cooled by conduction through the bond pad.

A third typical feature is visible if the temperature range is tightened around the substrate temperature, as shown in Figure 5.6. Here, the tortuous path taken by heat from the beam to the substrate is clearly visible. Because the thermal conductivity of oxide is more than an order of magnitude lower than that of polysilicon, the heat preferentially flows in the latter material. Because the trapped oxides and process constraints prevent lining up the trenches, the thermal resistance of the overall structure is appreciable. This resistance is visible in the temperature profiles shown in subsequent sections as an offset from the ambient value at the beam base.

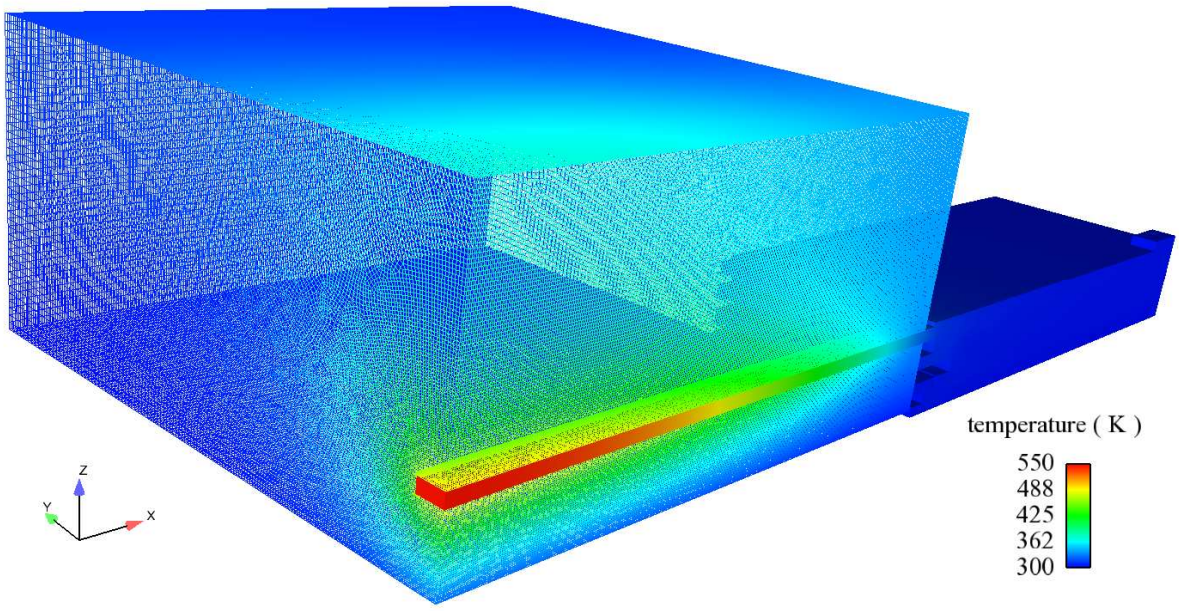

Figure 5.5. Temperature field for Case 16 with unity accommodation.

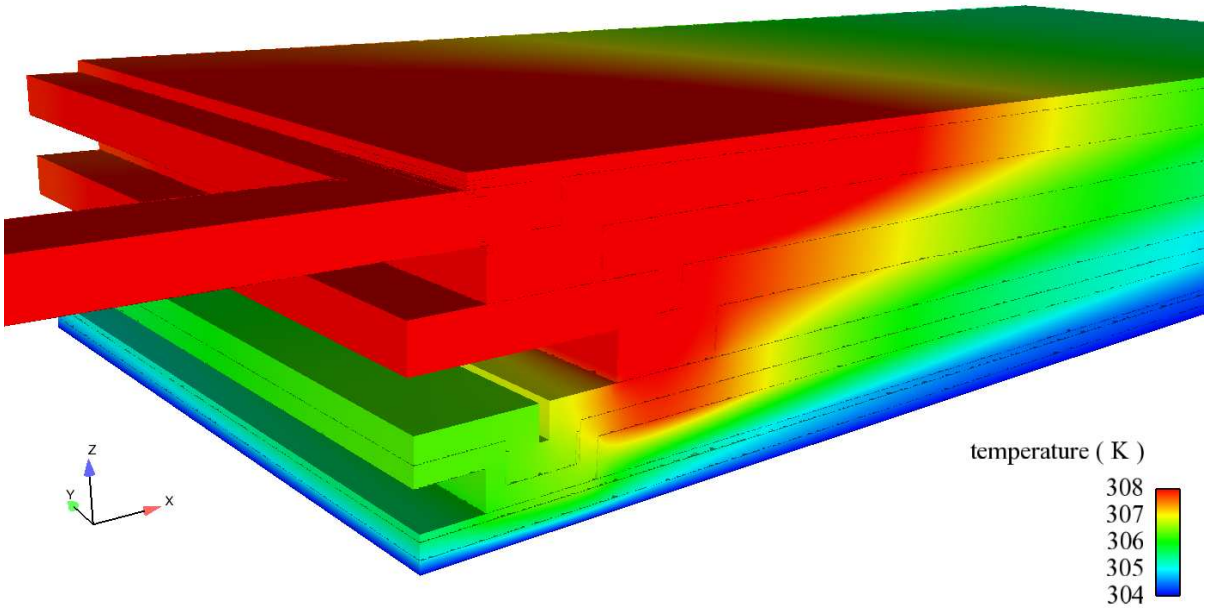

Figure 5.6. Bond-pad temperature field with reduced color range.

5.4. Simulation and Experimental Temperature Profiles

The combined gas-solid heat-transfer model described in previous sections is applied to compute temperature profiles corresponding to the previously presented experimental results. Figures 5.7 and 5.8 show the calculated and measured temperature profiles for the 200 μm and 400 μm beams, respectively. Several points must be understood in order to draw appropriate conclusions from these figures.

1. Each plot in each figure contains all model and experimental temperature profiles for the same beam length and the same gas pressure.

2. Each 200 μm plot contains temperature profiles for two powers ("high" and "low"), whereas each 400 μm plot contains temperature profiles for only one power ("low"). The high-power and low-power conditions produce maximum temperatures of ~600 K and ~450 K, respectively. The 625 torr 200 μm plot is divided into two separate plots for reasons discussed below. The leftmost 625 torr 200 μm plot contains an additional power ("medium"). The colors red, green, and blue denote high, medium, and low, respectively.

3. For each combination of beam length, gas pressure, and power, three model temperature profiles are presented, corresponding to accommodation coefficients of 1.0, 0.3, and 0.0. A value of 1.0 produces the maximum gas heat transfer possible, a value of 0.0 produces the minimum gas heat transfer possible (namely, zero), and the intermediate value of 0.3 is a low value compared to measurements (Saxena and Joshi, 1989; Trott et al., 2009).

4. The thermal conductivity of polysilicon depends strongly on the crystal structure, which can vary between processing runs and change over time, especially at high temperatures. As described in Section 4.3, the temperature-dependent thermal conductivity in Equation 4.12 includes a temperature-independent offset selected to make the red model curve pass through the topmost red symbols in the upper-left plot of Figure 5.7. This high-power low-pressure case was used because the full temperature range is accessed and the gas heat transfer is essentially zero so that only the solid properties are important. This "calibrated" temperature-dependent thermal conductivity (Equation 4.12) lies within the reported measurement uncertainty (15%) and is used without modification in all simulations.

5. This calibration approach can be assessed to some degree by examining the low-power low-pressure temperature profiles, the blue values in the upper-left plot of Figure 5.7. The model predicts the maximum temperature rise reasonably well but systematically overpredicts the temperature rise near the beam ends. This difference is not as visible in the two low-pressure 400 μm cases (low-power) of Figure 5.8, for which the simulation curves lie within the error bars for the entire temperature distribution.

6. Experimental artifacts are clearly visible in the two 625 torr plots in Figure 5.7. The maximum temperature rises of the profiles in the right plot are roughly 40% larger than the corresponding values of the profiles in the left plot despite the fact that the powers are almost identical. The experimental results in the right plot are the first three data sets that are reported: Cases 6, 7, and 8. Apparently, something happened between Case 8 and Case 10 that altered the thermal behavior of the beams significantly and permanently.

7. As the pressure increases from 0.05 torr to 0.5 torr and to 5 torr, the three model profiles for each condition are seen to separate, which indicates the increasing importance of gas heat transfer as the pressure increases although gas heat transfer is not large yet. The high-power model and experimental profiles in these three plots of Figure 5.7 agree well. However, this agreement is not unexpected because the model is calibrated to match the 0.05 torr high-power profile and because gas heat transfer is still quite small below 5 torr. For the low-power profiles in these plots, the model again slightly overpredicts the temperature rise near the beam ends and also slightly underpredicts the maximum temperature rise by a progressively greater amount as the pressure is increased.

8. As the pressure increases to 50 torr, the agreement between the model and experimental profiles degrades, particularly for the low-power cases. At this pressure, the mean free path of gas molecules is about 1 μm, which is comparable to the beam thickness. This is the regime in which the gas-solid heat-transfer-coefficient model is expected to be least accurate. However, the differences are more than what would be expected based on the comparisons of molecular and FEM gas simulations. An accommodation coefficient of 0.3 would represent the high-power profile well and the low-power profile marginally, but this value is much lower than expected (Saxena and Joshi, 1989; Trott et al., 2009).

9. At a pressure of 625 torr (ambient), the experimental profiles are divided into two groups, Cases 10 and 29-30 (bottom left plot) and Cases 6-8 (bottom right plot). The model and experimental profiles agree well for Cases 10 and 29-30 but differ for Cases 6-8. Again, this is not a defect of the model; rather, the experimental results differ significantly between themselves. Since the model is calibrated using Case 26, it is reasonable that the model agrees more closely with the later cases than with the earliest cases.

10. For most low-power profiles in Figure 5.7, the model overpredicts the experimental temperatures near the beam ends and underpredicts the experimental maximum temperature rise. One possibility suggested by this observation is that the experimental thermal conductivity is larger at ambient temperature but decreases more rapidly with increasing temperature than the thermal conductivity used in the model.

11. The model and experimental 400 μm temperature profiles are in reasonable agreement although the agreement degrades as the gas pressure is increased. These profiles are all low-power and are similar to those of the 200 μm beams. The systematic differences between the 200 μm low-power experimental and simulation profiles are present in some of the 400 μm data sets as well but to a lesser extent.

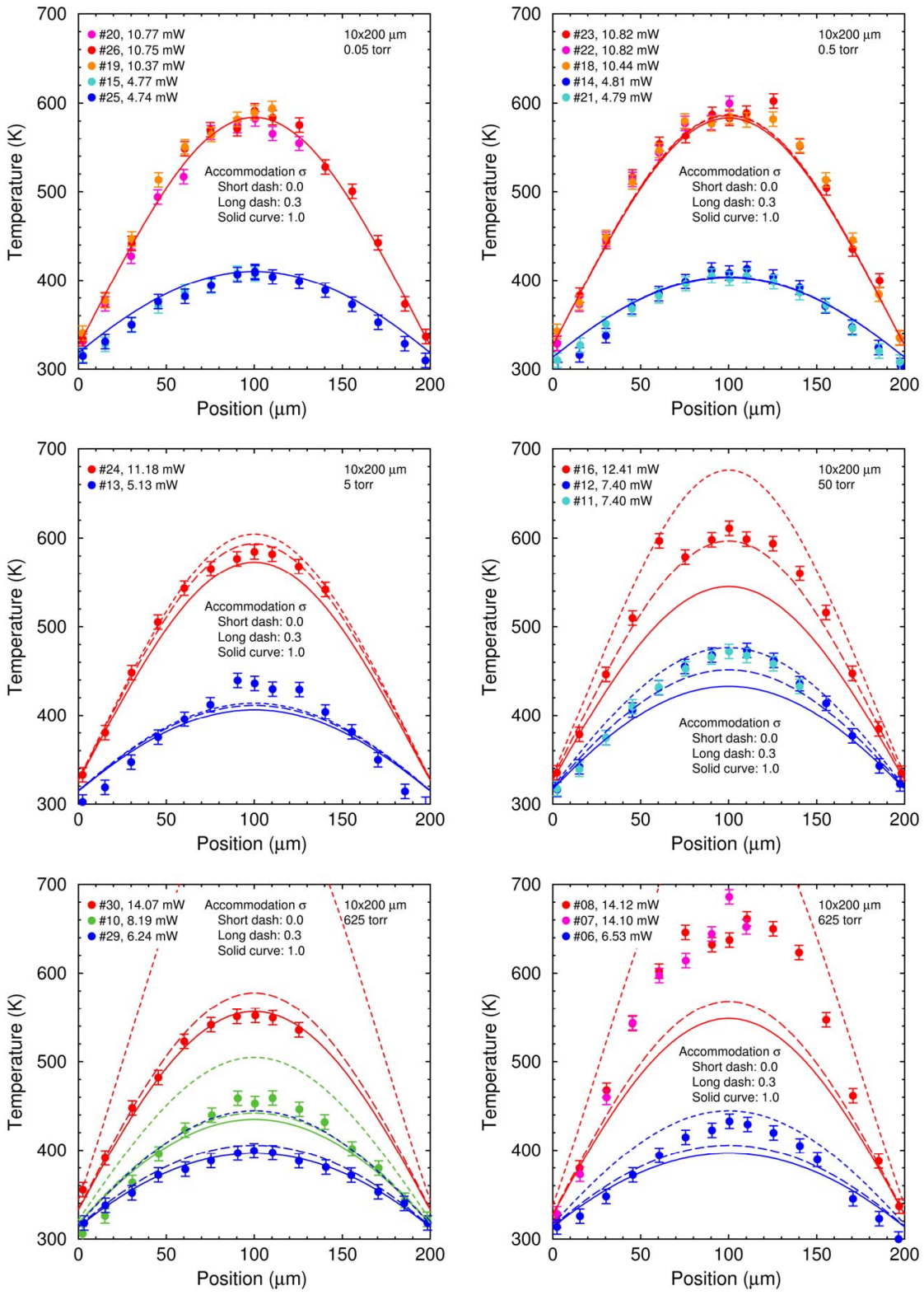

Figure 5.7. Comparison of experimental and simulation 200-μm temperature profiles.

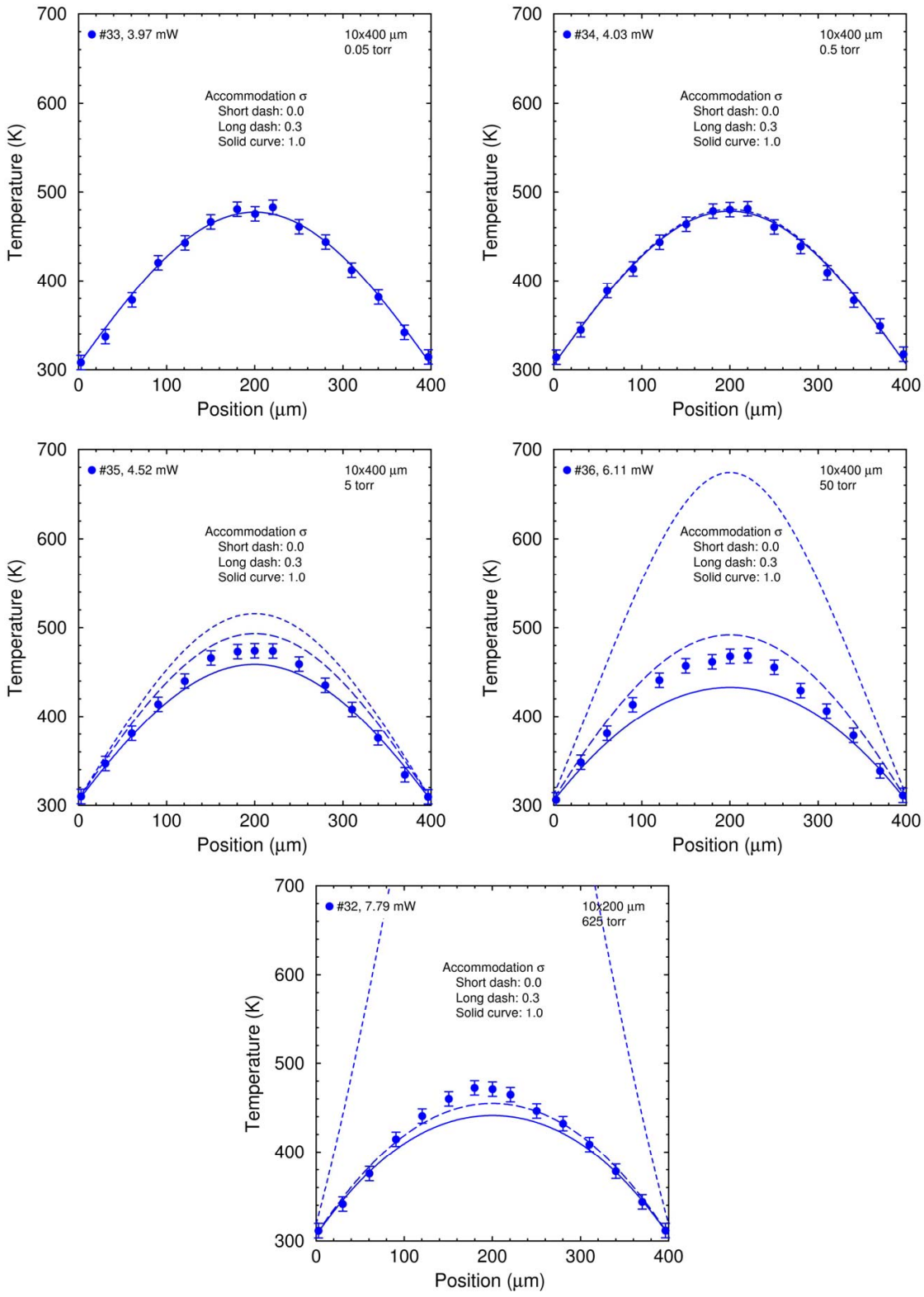

Figure 5.8. Comparison of experimental and simulation 400-μm temperature profiles.

5.5. Simulation and Experimental Electrical Results

Because the thermal conductivity and the electrical conductivity are both functions of temperature, the observed electrical properties of the device provide another means of comparison between simulation and experiment. In both simulation and experiment, a specified current is applied, and the resulting voltage drop is measured. The simulation and experimental values are plotted for the 200 μm beam cases in Figure 5.9.

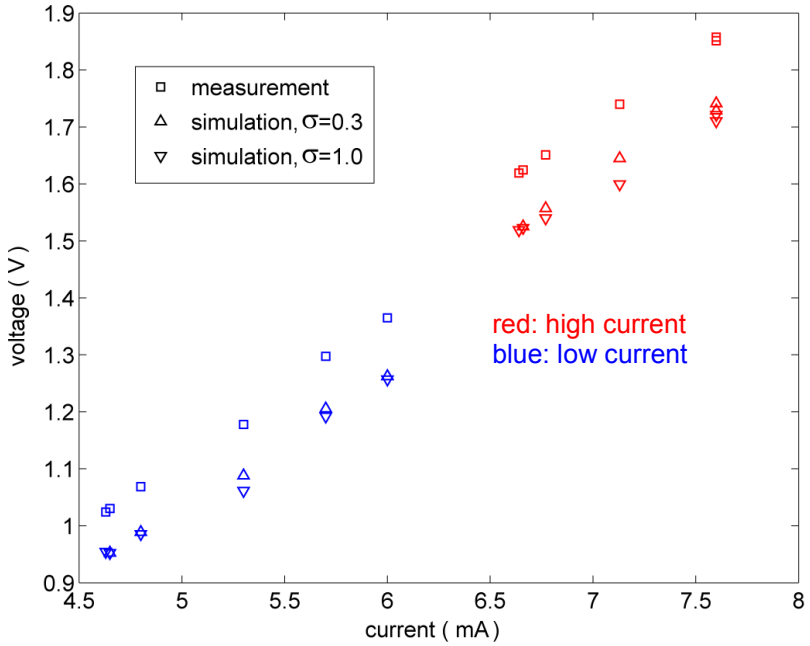

Figure 5.9. Experimental and simulation voltage drop vs. current for 200 μm beam.

The first of several features of interest in Figure 5.9 is that, within a respective data set, the values appear largely linear, despite the nonlinear relationship between temperature and current. This is a consequence of the experimental design, whereby the current was adjusted at a given pressure to achieve a roughly constant maximum temperature within each data set. Some nonlinearity does exist, however, due to the subtle differences in the temperature profiles, owing to the changing balance between heat conduction along the solid beam and heat conduction through the gas as the pressure is varied.

A second notable feature in Figure 5.9 is that the high-current and low-current data sets do not appear to be collinear. This feature is also related to the experimental design. The high-current and low-current data sets were adjusted to differing maximum temperatures. The average temperature in the beam, and therefore the average resistance, differs between these data sets. The slightly larger apparent slope of the high-current cases is consistent with a larger average resistance, which, owing to the positive slope of the temperature-resistance relation for this material, is consistent with a higher temperature.

A third feature clearly present in Figure 5.9 is an almost constant difference between the voltages observed in the simulation and in the experiment. This offset is a consequence of additional resistance present in the experiment due to connections, wires, and instrumentation, as

described in Phinney et al. (2007). In the thermal-conductivity experiments detailed in Phinney et al. (2007), the offset resistance was estimated to be approximately 19 Ω via a curve-fitting procedure outlined in that work. In the current work, which relies on a different apparatus, an offset resistance of roughly 16 Ω is observed.

A fourth feature in the electrical data is the notable dependence on the thermal accommodation coefficient σ, with a higher value corresponding to a lower observed voltage. This is again related to the temperature distribution in the beam because a higher value produces a lower temperature at a given pressure. The dependence of temperature on the thermal accommodation coefficient σ, as observed in the previous section, is a non-monotonic function of pressure. At very low pressures, the temperature is insensitive to σ because the gas is a weak conductor. At very high pressures, the temperature is insensitive to σ because the Knudsen layer, where σ is important, occupies a relatively small region near the solid. At intermediate pressures, the temperature is sensitive to σ because the gas carries a significant portion of the heat and the Knudsen layers occupy a significant portion of the domain.

6. CONCLUSIONS

To satisfy the completion criteria of ASC Level 2 Milestone 2841, a computational gas-solid heat-transfer model has been developed and applied to calculate temperature profiles for SUMMiT V RS539 Mod5 P4 fixed-fixed beam test structures similar to thermal-actuator legs. The calculated temperature profiles have been compared to experimental temperature profiles measured by another project. In general, the model does an adequate job in predicting maximum temperature rises of these beams at the specified powers although some differences are observed. Several observations can be made based on this exercise.

1. The Sandia ASC code Calore can be used to compute coupled gas-solid heat transfer with electrical heating for complex three-dimensional microstructures, where noncontinuum effects for the gas and the solid are included.

2. Having accurate material properties for polycrystalline silicon is the first of the two main impediments to being predictive. In particular, the thermal conductivity depends on the grain-size distribution, which depends on the fabrication process and the thermal history. The electrical resistivity and the thermal accommodation coefficient have similar issues. It is noted that these quantities are quite difficult to measure or to compute.

3. Having accurate geometric properties for polycrystalline silicon devices is the second of the two main impediments to being predictive. In particular, layer thicknesses need to be provided based on measurements made routinely during processing or measurements made on the devices under investigation (or perhaps on dedicated test structures).

4. Experiments can have their own issues. Operation under conditions such as prolonged elevated temperatures can change material properties significantly in an uncontrolled and nonuniform fashion and can perhaps change geometric properties like the beam-substrate gap height as well.

It is recommended that future efforts focus on addressing these issues, especially how to determine accurate geometric properties for a particular polysilicon device and accurate material properties for a particular polysilicon sample, including its interaction with the surrounding gas.

APPENDIX A. SAMPLE CALORE INPUT DECK

This input deck is designed to be run through the application APREPRO, which is installed wherever the SIERRA codes are available. This application allows the substitution of the named variables listed at the top into their appropriate positions throughout the input deck, greatly easing setup for the many cases examined in this work.

```
# CASE 23
# REFTEMP =   { REFTEMP   = 30+273   } K
# CURRENT =   { CURRENT   = 5.40     } mA
# PRESSURE  = { PRESSURE  = 83326.25 } Pa
# ACCOMCOEF = { ACCOMCOEF = 1.0      }
# BEAMWIDTH = { BEAMWIDTH = 9.65     } um
# BEAMTHICK = { BEAMTHICK = 2.33     } um
# GAP       = { GAP       = 11.872   } um

Begin sierra
Title P&EM Milestone

user subroutine file is gasbc.f

begin finite element model solid_thermal
   Database Name = b10x200_solid_med.g
   use material aluminum for block_1
   use material polysi for block_2 block_4 block_6 block_8 block_10
   use material oxide  for block_3 block_5 block_7 block_9 block_12
   use material nitride for block_11
end

begin finite element model solid_electro
   Database Name = b10x200_elec_med.g
   use material alum_electro for block_1
   use material polysi_electro for block_2
end

begin finite element model gas
   Database Name = b10x200_gas_med.g
   use material nitrogen for block_1
end

begin definition for function conductivity_si_elec
   type is analytic
   evaluate expression is "1 / (0.0232*x + 13.6997);"  # 1/ (ohm um)
end

begin definition for function THERMAL_CONDUCTIVITY_A
   type is analytic
   evaluate expression is "1e-6/(0.0066+.00116*(0.03*x-2))-6.5e-6;"
end

begin property specification for material polysi
   Thermal Conductivity Function = THERMAL_CONDUCTIVITY_A
   density = 1
   specific heat = 0
end

begin property specification for material polysi_electro
   thermal conductivity user variable = user_var_temperature function = conductivity_si_elec
   density = 1
   specific heat = 0
```

```
end

begin property specification for material aluminum
   Thermal Conductivity = 235e-6 $(W / um K)
   density = 1
   specific heat = 0
end

begin property specification for material alum_electro
   Thermal Conductivity = 35.7143  $(1 / Ohm um)
   density = 1
   specific heat = 0
end

begin property specification for material nitride
   Thermal Conductivity = 3.2e-6 $(W / um K)
   density = 1
   specific heat = 0
end

begin property specification for material oxide
   Thermal Conductivity = 1.4e-6 $(W / um K)
   density = 1
   specific heat = 0
end

### Nitrogen ###
begin property specification for material nitrogen
   thermal conductivity function = gas_k
   density = 1
   specific heat = 0
end

Begin Definition for Function gas_k
   Type = analytic
  $ need W / um K
   evaluate expression is "1e-6*1.3115075e-5*pow(x,1.6223709)/(1+1.427919e-2*x);"  $Torczynski
End

Begin Definition for Function gas_mu
   Type = analytic
   evaluate expression is "1.2594024e-8*pow(x,1.5044133)/(1+9.1694406e-3*x);"  $Torczynski
End

Begin Definition for Function gas_nint
   Type = piecewise linear
   Begin values
      0           2.
      300.0000    2.0000
      325.0000    2.0054
      350.0000    2.0121
      375.0000    2.0189
      400.0000    2.0323
      450.0000    2.0660
      500.0000    2.1132
      550.0000    2.1738
      600.0000    2.2412
      650.0000    2.3152
      700.0000    2.3961
      750.0000    2.4769
      800.0000    2.5577
      850.0000    2.6386
      900.0000    2.7194
      950.0000    2.7935
```

```
   End values
End

Begin Definition for Function gas_const
   type is constant
   begin values
       296.9140476886141  # (J/ kg K)
   end
end

# Set up post-processors so we can monitor approach to steady state
 Begin Calore Field Function tempdotfunc
    Use Nodal Field temperatureDot
 End

begin average value postprocessor ave
   use function tempdotfunc
   volumes block_2           # Poly4
end

begin postprocessor output control
    write to file post.dat
 end

begin output scheduler outsched
   start time = 0
   At Step 0, Increment = 1
   output on signal is Sigterm
   output on signal is Sigkill
end

#########################################################################
#                              LINEAR SOLVER
#########################################################################
Begin trilinos Equation Solver solve
   Solution Method = cg
   Preconditioning Method = dd-ilu
   Maximum Iterations  = 2000
   Residual Norm Tolerance = 1e-10
   Residual Norm Scaling = r0
End

begin calore procedure CalProcedure

#########################################################################
#                              SOLUTION CONTROL
#########################################################################
     begin solution control description

       begin system main

          begin transient stepper
             advance calore_electrical
             transfer elec_to_solid

             advance calore_solid_thermal
             transfer solid_to_gas

             advance calore_gas_thermal
             transfer gas_to_solid

             advance calore_solid_thermal
             transfer solid_to_elec
```

```
            execute postprocessor group tdot on calore_solid_thermal
          end

       end system main

       use system main

       begin parameters for transient stepper
         start time = 0.0
         converged when "CURRENT_STEP >= 2 && abs(ave) < 1e-8"
         begin parameters for calore region calore_solid_thermal
            transient step type is automatic
            time step is 1e-1
         end
      end

     end solution control description

#####################################################################
#                              TRANSFERS
#####################################################################
begin transfer elec_to_solid
   interpolate volume nodes from calore_electrical to calore_solid_thermal
   send block block_1 block_2 to block_1 block_2
   send field ohm_heat state none to ohm_heat_integrated state none
end

begin transfer solid_to_elec
   interpolate volume nodes from calore_solid_thermal to calore_electrical
   send block block_1 block_2 to block_1 block_2
   send field temperature state new to user_var_temperature state none
end

begin transfer gas_to_solid
   interpolate surface nodes from calore_gas_thermal to calore_solid_thermal
   send block surface_10 surface_11 surface_12 to surface_10 surface_11 surface_12
   send field h state none to h state none
   send field temperature state new to gastemp state none
end

begin transfer solid_to_gas
   interpolate surface nodes from calore_solid_thermal to calore_gas_thermal
   send block surface_10 surface_11 surface_12 to surface_10 surface_11 surface_12
   send field temperature state new to solidtemp state none
end

#####################################################################
#                              ELECTRICAL REGION
#####################################################################
   begin Calore region calore_electrical

      number of nonlinear steps = 1000
      nonlinear convergence tolerance = 1.0E-15
      Nonlinear Relaxation Factor = 1.0

      use finite element model solid_electro
      use linear solver solve

      calculate ohmic heating

      Begin User Variable user_var_temperature
         type = node real
         initial value = {REFTEMP}
      End User Variable user_var_temperature
```

```
      begin temperature boundary condition voltage_bc_1
         temperature = 0.0 # volts
         add surface surface_2
      end temperature boundary condition

      Begin Heat Flux Boundary Condition current_density
         flux = {CURRENT}e-5  # A/um^2  (current lands are 50 um2)
         add surface surface_1
      End

      Begin Surface Power Output incurrent
         add surface surface_1
      End

      Begin Surface Power Output outcurrent
         add surface surface_2
      End

     Begin Results Output Label out
         database Name = elec.e
         use output scheduler outsched
         Nodal Variables = recovered_gradient as Efield
         Nodal Variables  = temperature as voltage
         Nodal Variables  = ohm_heat
         global variables = incurrent
         global variables = outcurrent
      end

   end Calore region calore_electrical


######################################################################
#                            SOLID THERMAL REGION
######################################################################
   Begin Calore Region calore_solid_thermal

      begin postprocessor group tdot
         evaluate postprocessor ave
      end

      number of nonlinear steps = 1000
      nonlinear convergence tolerance = 1.0E-15
      Nonlinear Relaxation Factor = 1

      Use Finite Element Model solid_thermal
      Use Linear Solver solve

      Begin Initial condition ICblock_0
         temperature = {REFTEMP}
         all volumes
      End

      Begin user variable h
         type = node real length = 1
         initial value = 0
      End

      Begin user variable gastemp
         type = node real length = 1
         initial value = {REFTEMP}
      End

      Begin convective flux boundary condition beamflux
```

```
         add surface surface_10 surface_11 surface_12
         convective coefficient node variable is h
         reference temperature  node variable is gastemp
         integrated power output beampower_solid
      End

      Begin User Variable ohm_heat_integrated
         type = node real
         initial value = 0.0
      End User Variable ohm_heat_integrated

      Begin volume heating ohm_heat
         nodal variable = ohm_heat_integrated
         add volume block_1 block_2
      End volume heating ohm_heat

      begin temperature boundary condition blah
         temperature = {REFTEMP}
         add surface surface_8
      end

      Begin Results Output Label out
         Database Name is solid.e
         Nodal Variables = temperature
         use output scheduler outsched
      End

   End Calore Region calore_solid_thermal


######################################################################
#                            GAS THERMAL REGION
######################################################################
   Begin calore region calore_gas_thermal

      use finite element model gas
      use linear solver solve

      number of nonlinear steps = 1000
      nonlinear convergence tolerance = 1.0E-15
      Nonlinear Relaxation Factor = 1.0

#                  pressure(Pa)
      real data     {PRESSURE}

      Begin Initial Condition ic1
         temperature = {REFTEMP}.
         all volumes
      End

     begin nodal source beamtop
         add surface surface_10
         node subroutine is gasbc_ginf

         #         accom coef      width
         real data {ACCOMCOEF}  {BEAMWIDTH}
      end

      begin nodal source beamside
         add surface surface_11
         node subroutine is gasbc_ginf

         #          accom coef     width
         real data  {ACCOMCOEF} {BEAMTHICK}
```

```
      end

      begin nodal source beambottom
         add surface surface_12
         node subroutine is gasbc

         #          accom coef     width     gap
         real data  {ACCOMCOEF} {BEAMWIDTH} {GAP}
      end

      begin nodal source substrateunderbeam
         add surface surface_13
         node subroutine is gasbc
         #          accom coef   width      gap
         real data  {ACCOMCOEF} {BEAMWIDTH} {GAP}
      end

      begin nodal source substrate
         add surface surface_14
         node subroutine is gasbc_gwinf
         #          accom coef
         real data {ACCOMCOEF}
      end

      Begin user variable h
         type = node real length = 1
         initial value = 0
      End

      Begin user variable solidtemp
         type = node real length = 1
         initial value = {REFTEMP}
      End

      Begin convective flux boundary condition beamflux
         add surface surface_10 surface_11 surface_12
         convective coefficient node variable is h
         reference temperature  node variable is solidtemp
         integrated power output beampower_gas
      End

      Begin convective flux boundary condition substrateflux
         add surface surface_13 surface_14
         convective coefficient node variable is h
         reference temperature is {REFTEMP}
         integrated power output substratepower
      End

      begin results output label out
         database name = gas.e
         use output scheduler outsched
         nodal variables = temperature
         nodal variables = h
      end

   End  calore region calore_gas_thermal

end calore procedure CalProcedure

end sierra
```

APPENDIX B. USER SUBROUTINE FOR GAS MODEL

The user subroutine implementing the noncontinuum gas-solid boundary condition is listed below. Two additional versions were used for situations where the gap was infinite and where both the gap and the width were infinite. In these versions, the final expression was modified to build in the proper limits, rather than multiplying by or, worse yet, dividing by zero.

```
c     this is a node-based subroutine
      subroutine gasbc( nodeID, nNode, coords, nullValue, ierror)
c
c     calculate convection coefficient as a function of constant
c     wall temperature
c
      implicit none

      integer nNode, ierror, found
      integer nodeID(nNode)
      double precision coords(3,nNode), nullValue(nNode)

      double precision C1, C2, C3, C4, C5
      parameter (C1=0.167, C2=0.599, C3=1.23, C4=0.32, C5=1.02)

C     Pi / 2
      double precision M_PI_2
      parameter (M_PI_2=1.5707963267948966192 3D0)

      integer iNode
      double precision rdata(3)
      double precision press, gasconst, accom, width, gap
      double precision temp, visc, nint
      double precision mfp, s, coef

C     get region data for pressure and gas constant
      call acal_get_region_real_data(1,rdata)

C     gas pressure
      press = rdata(1)

C     gas constant
      call acal_get_function_values( 1, 1d0, gasconst, 9 ,'gas_const')

C     get instance data for accommodation coefficient and geometry
      call acal_get_instance_real_data(3,rdata)

C     accommodation coeficient
      accom = rdata(1)

C     width
      width = rdata(2)*1e-6

C     gap
      gap   = rdata(3)*1e-6

      do iNode = 1, nNode

C        Set the return value to zero, because we don't actually want
C        a nodal source (we're just hijacking the mechanism to get the
C        nodal variable we're after)
         nullValue(iNode) = 0.
```

```
    call acal_get_pred_nodal_t( nodeID(iNode), temp, found )

    call acal_get_function_values( 1, temp, visc, 6 ,'gas_mu')

    call acal_get_function_values( 1, temp, nint, 8 ,'gas_nint' )

    mfp = sqrt(M_PI_2*gasconst*temp)*visc/press

    s = 2 - accom + accom/(1 + C4*width/gap + C5*width/mfp)

    s = s*(1+ C1*accom / (1 + C2*mfp/gap + C3*mfp/width ))

    coef = (1+0.25*nint)*(accom/s)*(2*gasconst*visc/mfp)*1e-12

    call acal_put_real_nodal_var( coef, nodeID(iNode), 1,
&                                 'h', found )

 end do

 ierror=0

 return
 end
```

REFERENCES

Arkilic et al., 2001: E. B. Arkilic, K. S. Breuer, and M. A. Schmidt, "Mass Flow and Tangential Momentum Accommodation in Silicon Micromachined Channels," *Journal of Fluid Mechanics*, Vol. 437, pp. 29-43, 2001.

Aspnes and Studna, 1983: D. E. Aspnes and A. A. Studna, "Dielectric Functions and Optical Parameters of Si, Ge, GaP, GaAs, GaSb, InP, InAs, and InSb from 1.5 to 6.0 eV," *Physical Review B*, Vol. 27, No. 2, pp. 985-1009, 1983.

Aubry et al., 2007: S. Aubry, C. J. Kimmer, L. M. Phinney, E. S. Piekos, P. K. Schelling, and E. B. Webb, III, "Phonon-Mediated Thermal Transport in Microsystems," Sandia report, SAND2007-6622, Sandia National Laboratories, Albuquerque, NM, 2007.

Aubry et al., 2008: S. Aubry, C. Kimmer, A. Skye, P. K. Schelling, "Comparison of Theoretical and Simulation-Based Predictions of Grain Boundary Kapitza Resistance in Silicon", *Physical Review B*, in press, 2008.

Bartel et al., 2001: T. J. Bartel, S. J. Plimpton, and M. A. Gallis, *Icarus: A 2-D Direct Simulation Monte Carlo (DSMC) Code for Multi-Processor Computers*, User's Manual, Version 10.0, Sandia report SAND2001-2901, Sandia National Laboratories, Albuquerque, NM, 2001.

Beechem et al., 2007: T. Beechem, S. Graham, S. P. Kearney, L. M. Phinney, and J. R. Serrano, "Simultaneous Mapping of Temperature and Stress in Microdevices Using Micro-Raman Spectroscopy," *Review of Scientific Instruments*, Vol. 78, No. 6, pp. 061301, 2007.

Bird, 1994: G. A. Bird, *Molecular Gas Dynamics and the Direct Simulation of Gas Flows*, Clarendon Press, Oxford, UK, 1994.

Calore, 2006: S. W. Bova, K. D. Copps, and C. K. Newman, *Calore: A Computational Heat Transfer Program, Volume 1: Theory Manual*, Sandia report SAND2006-6083P, Sandia National Laboratories, Albuquerque, NM, 2006.

Calore, 2008: Calore Development Team, *Calore: A Computational Heat Transfer Program, Volume 2: User Reference Manual*, Version 4.6, Sandia report SAND2008-0098P, Sandia National Laboratories, Albuquerque, NM, 2008.

COMSOL, 2008: COMSOL Multiphysics, User's Guide, Version 3.4, http://www.comsol.com/, Stockholm, Sweden, 2008.

Gallis et al., 2007: M. A. Gallis, J. R. Torczynski, and D. J. Rader, "A Computational Investigation of Noncontinuum Gas-Phase Heat Transfer Between a Heated Microbeam and the Adjacent Ambient Substrate," *Sensors and Actuators A*, Vol. 134, No. 1, pp. 57-68, 2007.

Graham et al., 2003: S. Graham, B. Olson, C. C. Wong, E. S. Piekos, A. McConnell, and K. E. Goodson, "The Effects of Processing Conditions on the Thermal Conductivity of Polycrystalline Silicon Films, IMECE2003-42091, ASME, Washington, DC, 2003.

Holland and Neuringer, 1962: M. G. Holland and L. J. Neuringer, in Proceedings of the International Conference on the Physics of Semiconductors, Exeter, The Institute of Physics and The Physical Society, London, p. 475, 1962.

Hull, 1999: R. Hull, editor, *Properties of Crystalline Silicon*, EMIS Data Reviews Series No. 20, B. L. Weiss, series advisor, INSPEC, London, UK, 1999.

Jorgensen et al., 2001: C. R. Jorgensen and V. R. Yarberry, "A 3D Geometry Modeler for the SUMMiT V™ MEMS Designer," Fourth International Conference on Modeling and Simulation of Microsystems (MSM 2001), Hilton Head, SC, March 19-21, 2001.

Kearney et al., 2006: S. P. Kearney, L. M. Phinney, and M. S. Baker, "Spatially Resolved Temperature Mapping of Electrothermal Actuators by Surface Raman Scattering," Journal of MicroElectroMechanical Systems, Vol. 15, No. 2, pp. 314-321, 2006.

Kremer et al., 2004: R. K. Kremer, K. Graf, M. Cardona, G. G. Devyatykh, A. V. Gusev, A. M. Gibin, A. V. Inyushkin, A. N. Taldenkov, and H.-J. Pohl, "Thermal Conductivity of Isotopically Enriched ^{28}Si: Revisited," *Solid State Communications*, Vol. 131, No. 8, pp. 499-503, 2004.

McConnell et al., 2001: A. McConnell, S. Uma, and K. E. Goodson. "Thermal Conductivity of Doped Polysilicon Layers," *Journal of Microelectromechanical Systems*, Vol. 10, No. 3, pp. 360-369, 2001.

Paul et al., 1994: O. M. Paul, J. Korvink, and H. Baltes, "Determination of the Thermal Conductivity of CMOS IC Polysilicon," *Sensors and Actuators A*, Vol. 41, Nos. 1-3, pp. 161-164, 1994.

Phinney et al., 2006: L. M. Phinney, J. D. Kuppers, and R. C. Clemens, *Thermal Conductivity Measurements of SUMMiT V Polycrystalline Silicon*, Sandia report SAND2006-7112, Sandia National Laboratories, Albuquerque, NM, 2006.

Phinney et al., 2007: L. M. Phinney, E. S. Piekos, and J. D. Kuppers, "Bond Pad Effects on Steady State Thermal Conductivity Measurement Using Suspended Micromachined Test Structures," IMECE2007-41349, American Society of Mechanical Engineers, New York, NY, 2007.

Saxena and Joshi, 1989: S. C. Saxena and R. K. Joshi, *Thermal Accommodation and Adsorption Coefficients of Gases*, CINDAS Data Series on Material Properties, Vol. II-1, C. Y. Ho, series editor, Hemisphere Publishing Corporation, New York, NY, 1989.

Sniegowski and de Boer, 2000: J. J. Sniegowski and M. P. de Boer, "IC-Compatible Polysilicon Surface Micromachining," *Annual Review of Materials Science*, Vol. 30, pp. 299-333, 2000.

SUMMiT V, 2008: *SUMMiT V™ Five Level Surface Micromachining Technology Design Manual*, Version 3.1a, Sandia report SAND2008-0659P, Sandia National Laboratories, Albuquerque, NM, 2008.

Tanner, 2006: D. M. Tanner, private communication, Sandia National Laboratories, Albuquerque, NM, 2006.

Torczynski et al., 2005: J. R. Torczynski, C. C. Wong, E. S. Piekos, M. A. Gallis, D. J. Rader, and B. L. Bainbridge, *Modeling Microscale Heat Transfer Using Calore*, Sandia report SAND2005-5979, Sandia National Laboratories, Albuquerque, NM, 2005.

Trott et al., 2009: W. M. Trott, D. J. Rader, J. N. Castañeda, J. R. Torczynski, and M. A. Gallis, "Measurement of Gas-Surface Accommodation," *Rarefied Gas Dynamics: 26th International Symposium*, American Institute of Physics, Melville, NY, 2009.

White, 1984: F. M. White, *Heat Transfer*, Addison-Wesley Publishing Company, Reading, MA, 1984.

von Arx et al., 2000: M. von Arx, O. Paul, and H. Baltes, "Process-Dependent Thin-Film Thermal Conductivities for Thermal CMOS MEMS," *Journal of Microelectromechanical Systems*, Vol. 9, No. 1, pp. 136-145, 2000.

DISTRIBUTION

1	MS 0346	D. J. Rader	Org. 01513	
1	MS 0346	M. A. Gallis	Org. 01513	
1	MS 0346	P. E. Hopkins	Org. 01513	
1	MS 0346	L. M. Phinney	Org. 01513	
1	MS 0346	E. S. Piekos	Org. 01513	
1	MS 0346	J. R. Serrano	Org. 01513	
4	MS 0346	J. R. Torczynski	Org. 01513	
1	MS 0372	J. M. Redmond	Org. 01525	
1	MS 0384	A. C. Ratzel, III	Org. 01500	
1	MS 0824	T. Y. Chu	Org. 01500	
1	MS 0824	M. R. Prairie	Org. 01510	
1	MS 0825	C. W. Peterson	Org. 01510	
1	MS 0826	S. P. Kearney	Org. 01512	
1	MS 0833	C. L. Northrop	Org. 01055	
1	MS 1070	C. C. Wong	Org. 01526	
1	MS 1064	J. B. Wirth	Org. 02614	
1	MS 1064	E. J. Garcia	Org. 02614	
1	MS 1069	M. R. Platzbecker	Org. 017491	
1	MS 1080	M. J. Shaw	Org. 017491	
1	MS 1080	K. Ortiz	Org. 01749	
1	MS 0899	Technical Library	Org. 09536	(electronic copy)


Sandia National Laboratories